A Computational Model for Thin-Walled Structures with Variable Cross Sections

A THESIS
SUBMITTED TO THE FACULTY OF THE GRADUATE SCHOOL
OF THE UNIVERSITY OF MINNESOTA
BY

Ariel M. Dahl

IN PARTIAL FULFILLMENT OF THE REQUIREMENTS
FOR THE DEGREE OF
MASTER OF SCIENCE

Henryk K. Stolarski, Adviser

October 2011

ACKNOWLEDGMENTS

I would first like to thank the University of Minnesota and the Civil Engineering Department for letting me call it home for the last five years. I have thoroughly enjoyed my stay at the University, thanks to the support and friendship of my fellow graduate and undergraduate students and faculty members.

Specifically, I owe thanks to my adviser, Dr. Henryk Stolarski, who has been an amazing mentor throughout my graduate studies and whose many hours of guidance has made this research, and resulting thesis, possible. Additionally, I would like to thank Dr. Roberto Ballarini for encouraging me to pursue my master's degree as well as being instrumental in helping me get a fellowship through The Beavers, a heavy engineering construction association.

I would like to thank my committee members, Dr. Perry Leo and Dr. Steve Wojtkiewicz, for their time and energy serving on my committee. From the Fluids Group at SAFL, I have Dr. Fotis Sotiropoulos and Ph.D. student Toni Calderer to thank for their collaboration on the project, specifically by helping obtain funding from the DOE, as well as in coupling my code with theirs for full fluid-structure interaction. Also, my thanks to Brock Hedegaard who performed the shell model analysis using ABAQUS for this project.

Lastly, but certainly not least, I owe many thanks to my wonderful friends and family who have been very understanding of my time commitment to school and research. My mom, dad, and sister Kendra have all been more than supportive throughout my college career and who would have been proud of me no matter what I pursued. To my parents, it is you who taught me to always put my best foot forward, and it is you that I have to thank for the successful completion of my master's degree in engineering.

ABSTRACT

In this thesis, a computational thin-walled beam model is presented which can be used in various engineering applications and whose computer implementation is straightforward. The model is applicable to beams with both open and closed cross sections, including multicellular beams. The dimensions and topology of the beam's cross sections may arbitrarily (and possibly even abruptly) vary along the length of the beam. Anisotropic material properties are allowed, and they may vary both within the cross section and along the beam's length.

Compared to many existing models, the only assumption the model presented in this thesis retains is in-plane rigidity of the cross section. In particular, it does not require any definition of cross-sectional warping, which is typically needed in the present thin-walled beam models. Instead, in this model, a finite element mesh is used in which a carefully chosen set of degrees of freedom describes warping. The deformation pattern that this finite element mesh describes is superposed on the bending deformation described by Euler-Bernoulli beam theory. Consequently, in the model presented here the warping pattern is not predetermined but results from the solution of the final system of equations. This is particularly important for beams with variable cross section.

The presented model is tested through several numerical examples. Comparisons with independently obtained results, including the results obtained by much more sophisticated models, demonstrate the validity and accuracy of the formulation.

TABLE OF CONTENTS

LIST OF FIGURES

LIST OF TABLES

CHAPTER 1. INTRODUCTION

1.1 Motivation

Thin-walled (cold-formed) members are widely used in metal structures found in civil, aerospace, mechanical and other engineering applications. The shapes of their cross sections vary from simple (like angles, T-beams, I-beams) to complicated (various types of "channel" cross sections), particularly common in aluminum construction. One of the most important and characteristic features in the response of thin-walled beams (and columns) to mechanical loads is warping of their cross sections. This is very important as it affects the stress distribution in those structures as well as the maximum load that they can safely carry. In particular, the buckling load observed for these type of structures appears to be lower than that predicted by the well-known Euler formula. As a result, a serious research effort was undertaken, first experimental research and then research in the realm of mathematical modeling.

In this thesis, a model is presented which builds upon the findings of previous research, but does it in a way that is easily amenable to computer implementation. The model is somewhat more comprehensive than those presented previously (features of several models introduced earlier are included here in a single model), and is designed to be more convenient in numerical calculations, without loss of its accuracy and effectiveness. The model is applicable whenever a thin-walled structure needs to be analyzed, but the involvement of the author of this thesis in a project related to wind engineering (described later in Section 1.2) motivated the development presented herein. In this particular application, the blades of wind turbines are thin-walled structures, with multicellular cross sections which may vary along their length, whose individual parts are often built of different materials, which are frequently anisotropic. All those features should be allowed in a model to be useful in the analysis of turbine blades, but to the best knowledge of the author, a model incorporating all them has not been yet developed.

The research related to thin-walled beams and columns has a rather long history, but it has been particularly intensive in the last 50 years or so. For almost 30 of those years a technical journal specifically dedicated to the issues of thin-walled structures – "*Thin-Walled Structures*" – has been a main forum for publishing the research on the topic. The volume of related publications, found in that particular journal – as well as other technical publications – is very large, and it is impossible to review them in this thesis with the thoroughness they deserve. To justify the research undertaken in this thesis, and to outline its contribution, the reference will be made only to a relatively few publications in the area, mostly quite recent. However, those publications – and the references cited in them – should provide sufficient information for those interested in the subject to track all earlier developments related to thin-walled beams and columns.

In the area of modeling, the pioneering contribution addressing the behavior of thin-walled structures, was that of Russian scientist V.Z. Vlasov, originally published in 1959 [1], and made more commonly available in 1961 [2]. In his model, Vlasov complemented the Euler-Bernoulli beam model with functions describing torsion and warping of its cross section. He made the following main assumptions:

i. The cross section of the beam is rigid in its plane,
ii. The shear deformation in the plane tangent to the surface of the beam vanishes.

Based on those assumptions, a new system of one-dimensional differential equations describing the functions used in the description of the problem (transverse displacements and twist angle along the length of the beam) has been obtained. They required evaluation of some new cross-sectional parameters such as sectional moment of inertia, and products of inertia. While Vlasov's model did capture the main aspect of the thin-walled beams' behavior, it was presented in the context of prismatic beams of the so-called open cross section, and assumed constant isotropic properties of the material.

Following Vlasov's original idea, various extensions of his model have been subsequently proposed. In particular,

i. Shear deformations have been included [3,4,5].
ii. An approach to treat non-prismatic cross sections have been discussed in [6,7,8], including perforated beams [9].
iii. Formulation of the problems involving closed multicellular cross sections have been presented in [4,10].
iv. Anisotropic material properties have been included in [11,12].
v. Nonlinear analysis of thin-walled structures has been addressed in [7,8,10]

Many of the aspects listed above have been covered in a very comprehensive recent book, *"Thin-walled composite beams"* by L. Librescu [10], which - additionally - includes analysis of rotating thin-walled beams and control of their vibrations. None of the above publications, including the book by Librescu, account for all aspects needed in the analysis of wind turbine blades, which were described earlier in this section. In addition, the formulation of the problem in those contributions is such that a significant amount of work is needed before a computer implementation can be considered, as cross-sectional parameters have to be found ahead of time. How involving this task can be is readily seen by just perusing [10] or [11].

In most existing models, warping functions are predetermined using either Saint Venant theory, if the cross sections are closed, or Vlasov theory, when the cross sections are open. This is typically done assuming that the beam is prismatic and composed of a single isotropic material. The inclusion of anisotropic material properties necessitates a change in the way warping functions should be described, even for prismatic beams. In addition, functions determined that way often exclude additional warping that is due to the presence of resultant transverse shear forces. For beams with variable cross sections, no acceptable way of determining warping functions is available, let alone beams with variable cross sections and material properties. In this thesis, a computational model is developed that combines several features addressed in literature separately, and alleviates the aforementioned difficulties with the description of warping.

1.2 **Wind Engineering**

Wind power has become increasingly popular over the last 30 to 40 years as the public's desire for clean and renewable energy has become more pressing. Wind turbines are evolving faster today than ever before in terms of increasing size, newly engineered materials, highly complex instrumentation, and many other innovations. With this evolution and desire for more efficient energy harvesting, there is a pressing demand for research in all areas of wind engineering. Specifically, research in wind engineering includes everything from meteorology and noise reduction, to mechanical engineering of gear boxes, to composite materials and turbine manufacturing. The focus of this study is related to one aspect of that large spectrum of wind energy problems – the modeling of wind turbine blades. While the model developed here can be used in all thin-walled structures applications, it is hoped that its particular suitability will be in the analysis of air-turbine blade interaction and, ultimately, in structural blade design.

1.2.1 EOLOS & UMore Park

The research undertaken in this thesis was a small part of a large project funded by a 7.9 million dollar grant from the U.S. Department of Energy (DOE) to EOLOS, a University of Minnesota lead wind energy research consortium. The consortium was founded to promote "collaboration between the industry, universities, and governmental agencies that will lead to advances in wind energy technology, new innovation and long-term expansion of wind energy production in the United States," 0. Specifically, the consortium's goal is to support the DOE in their goal to increase the wind power contribution to the U.S. electrical supply from 2 to 20 percent by 2030.

EOLOS is currently focused on the construction of a 2.5 megawatt wind turbine that will be built in Minnesota's Dakota County at the University of Minnesota Outreach Research and Educational (UMore) Park. UMore Park consists of 5,000 acres of land purchased by the University with the goal of developing it into an entirely sustainable

community of about 20,000 to 30,000 residents within the next 25 to 30 years. The wind turbine is one example of how the University intends to use UMore Park as a means of promoting industry and academia collaboration toward increasingly efficient systems and innovative designs.

This study represents the first, and the major, step in the development of a computational (finite element) model for wind turbine blades. It is designed to be effective and practical for use in fluid-structure interaction (FSI) of the rotating turbine blades, after the effects of the overall rotation of the blade is incorporated in the model. Validation of the finite element model in its present form will be presented in Chapter 3, but the fully coupled FSI code, including overall rotation of the blade, is outside of the scope of this thesis. It will be developed and validated later by comparisons of simulated results with laboratory experiments. As the centerpiece of UMore Park, the 2.5 megawatt so called "Liberty" wind turbine will be used in the ultimate validation of the model.

1.3 **Models for Wind Turbine Blades**

Turbine blades are thin-walled structures with geometry varying along their length and possessing no axis of symmetry. For stability and strength reasons, their very small wall-thickness-to-global dimension ratio necessitates introduction of internal ribs extending in both the longitudinal and transverse directions. The complexity of that geometry is sufficiently large that all aspects of its structural behavior are unlikely to be captured by a simple model. Given that situation, the models developed for analysis of turbine blades should balance the complexity with purpose that they are meant to serve.

1.3.1 Shell Model

Shell models [14,15,16] are the most appropriate and most accurate models for thin-walled structures, and they are widely available in commercial computer codes such as ABAQUS, ANSYS, NASTYRAN, ADINA and other codes. These models are indispensable for examining local behavior of thin-walled structures, such as local buckling, precise local stress values, etc. However, these models are too elaborate and unnecessary for use in the coupled fluid-structure interaction analysis. From the structural point of view, the goal of this type of analysis is to determine the pressure applied to the structure involved, whose distribution and magnitude accounts for structural deformations. To achieve this goal, the local features such as local values of the strain and stress fields, patterns of local buckling modes or magnitudes of the stress level causing such buckling are immaterial, as long as the overall deformation of the structure is adequately described. In fact, in engineering applications, the structures interacting with fluids should be designed so as to eliminate the possibility of failure due to strength or stability reasons. Thus, the pressures obtained under assumptions that downplay local effects, but strive to correctly capture the overall deformation of the structure should be valuable from the point of view of the detailed structural design, which may involve more detailed structural models, such as shell models. It is possible to develop several more or less sophisticated structural models embedding such characteristics, and in this thesis, one such model is proposed.

1.3.2 Beam Models

Simple models of a structure that may undergo the general three-dimensional deformation – required in modeling of turbine blades – are various beam models using theories appropriate for solid beam cross sections. Even the simplest of them, the Euler Bernoulli beam model, has been used to analyze some deformation characteristics of wind turbine blades. However, beam models, including various higher-order beam models (such as Timoshenko's model, for example) do not incorporate warping, and do not adequately capture torsional properties of thin-walled beams. Both of those properties are essential features of thin-walled structure behavior.

There is a relatively large body of literature related to analysis of thin-walled beams [10]. It covers many different aspects specified as the goal for this thesis, such as multicellular cross sections [4,10], curved axis of the beam [3], but not all of them in a single model, which is needed for the purpose of the undertaken studies. In addition, all developments known to the author are based on the Vlasov theory or small modifications of it [eg. 3,4,11] and, as such, require independent computation of the sectional properties and warping functions, which appear as coefficients of the governing differential equations of those beams [10]. This is a serious drawback, particularly if the analysis needs to be repeated multiple times in an effort to find an optimal design of the beam (blade), or if the cross section consists of multiple segments with different geometry and/or material properties. Such a situation is typical in analysis of wind-turbine blades.

1.4 **Objectives**

While shell models very accurately capture the thin-walled nature of the wind turbine blades, the blades are so slender that their behavior is likely to be dominated by standard beam behavior. Acceptance of this view, as well as the view adopted in the previous sections, leads to a conclusion that development of a versatile computational model applicable to thin-walled beam-like structures is a worthwhile research topic. Thus, the objective of this thesis is the development of a computational, thin-walled beam model, which would be applicable to beams with open or closed cross sections, multicellular cross sections, beams whose cross sections vary along its length, and/or beams whose axis is (slightly) curved. The developed model should allow for different materials in various elements of cross sections. Furthermore, one of the objectives is that the proposed model should not require computation of the sectional properties such as moment of inertia, sectional moments of inertia, etc., which is a time consuming task, particularly for structures of variable cross section.

To achieve these goals, the proposed model combines the beam and finite element assumptions, and as a result, all sectional properties used in various beam theories are naturally and automatically incorporated in the analysis when the final system of equations is assembled.

The thin-walled beam model proposed in this study takes advantage of several geometric assumptions specific to the wind turbine blade, which allows for reduction in the system complexity and computation time. It attempts to achieve a balance between simplicity and accuracy so as to efficiently obtain accurate results when implemented in full fluid-structure interaction environment.

CHAPTER 2. THIN-WALLED BEAM MODEL

2.1 Basic Features of Model

2.1.1 Modeling Assumptions

Wind turbine blades are often constructed so as to have a small cross section dimension, d, relative to the length of the blade, L. Additionally, as illustrated in Figure 2-1, the ratio of the thickness of the wall, t, to the overall dimension of the cross section is much less than one. These two features of wind turbine blades allow us to make certain assumptions about the behavior of the blade and resulting stresses:

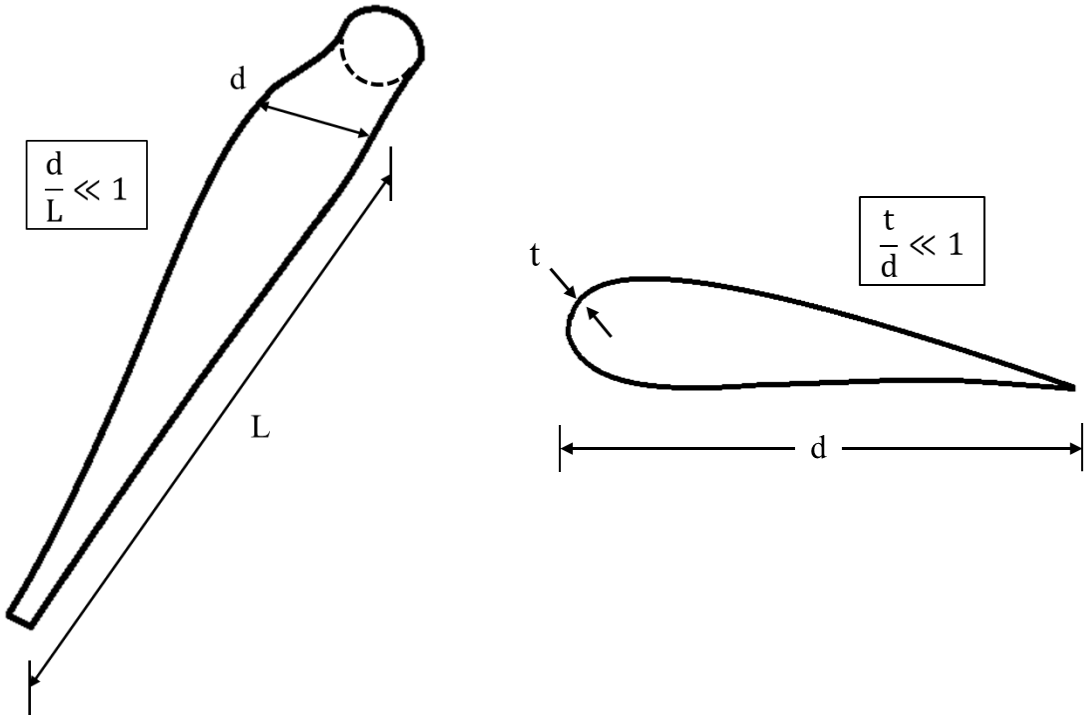

Figure 2-1: Geometrical Assumptions

A. Since the blades are typically slender, meaning that they have a small cross section overall dimension to length ratio, the motion of the wing will be dominated by beam behavior. In other words, beam bending and twisting will have the most significant impact on the resulting blade displacements. Furthermore, although this is not essential for the model and can be easily adjusted if needed, wind turbine blades are attached to the

tower structure solely at the hub, so the blades essentially act as cantilever beams with fixed boundary conditions at the location of the hub.

B. The walls of the blade are thin, so for closed cross sections we can neglect the variation of strain or stresses in the wall thickness direction and model the walls of the structure as a membrane. Only in-plane stresses are of interest (both normal and shear). [eg. 3,4] For open cross sections, variation of the in-plane shear stresses in the wall thickness direction is important. This can be accounted for by adding the well-known Saint Venant stiffness terms. [17]

C. The cross sections of the blade are assumed to be rigid in their planes (but they warp in the direction perpendicular to their planes). This assumption is not needed in the shell models of the blade, but it is justified in view of the fact that blades possess transverse ribs constraining the in-plane cross section deformation. In addition, cellular cross sections fixed at one end of the blade and closed at the other (as in the case of turbine blades) possess a rather high stiffness in the direction perpendicular to the axis of the beam, even if no transverse ribs exist.

D. Total deformation of the beam can be composed of its bending described by Euler-Bernoulli theory on which deformation due to warping is superimposed. One of the anticipated ramifications of describing the deformation process in this way is that neglecting inertia associated with warping degrees of freedom should have negligible effects on the dynamic response of the beams.

E. The cross section may not only be multicellular, but may vary along the length of the blade, including any abrupt changes. This is, in fact, a necessary requirement for a structure like a wind turbine blade that indeed has varying cross sectional dimensions along its length. This assumption necessitates a careful evaluation of strains in the model, particularly those related to warping and torsion. Furthermore, the internal walls of the blade – introduced to increase its stiffness and to enhance its stability properties – may terminate abruptly within the span of the blade.

2.1.2 Discretization and Degrees of Freedom

To conceptualize the discretization of the blade, first imagine a series of cross sections at regular intervals along the length of the blade that are perpendicular to an axis directed along its length. This defines a series of "slices" along the length of the blade. A number of nodes along the wall of the cross sections are then selected. Each cross section has the same number of nodes, so the nodes of neighboring cross sections can be connected. This forms a mesh of quadrilateral elements to be used in the model (of Figure 2-2).

The geometry of the quadrilateral surface element of Figure 2-2 can be described as follows

$$\begin{Bmatrix} x(\xi,\eta) \\ y(\xi,\eta) \\ z(\xi,\eta) \end{Bmatrix} = \begin{Bmatrix} \sum_{I=1}^{4} x_I \, N_I(\xi,\eta) \\ \sum_{I=1}^{4} y_I \, N_I(\xi,\eta) \\ \sum_{I=1}^{4} z_I \, N_I(\xi,\eta) \end{Bmatrix} \tag{2.1}$$

where

$$N_I(\xi,\eta) = \frac{1}{4}(1+\xi_I\xi)(1+\eta_I\eta) \tag{2.2}$$

are the basis functions associated with 4-node elements wherein $\xi_I,\eta_I \in \{-1,1\}$, $\xi,\eta \in [-1,1]$. The shape of the element obtained this way is not planar, and its edges are straight. It is over this non-planar surface element that the integration has to be performed to obtain the associated element (stiffness and mass) matrices. For this purpose the ξ,η non-orthogonal coordinate system introduced via Eq. ((**2.1**) is very convenient, and all integrated functions (components of strains, mean density, wall thickness, etc.) can be expressed in terms of ξ and η.

In accord with assumption D of Section **Error! Reference source not found.** the proposed thin-walled beam model considers two types of degrees of freedom: those associated with the behavior of the entire cross section (bending degrees of freedom) and nodal degrees of freedom with respect to the individual nodes within the cross section

which are parallel to the long axis of the blade (warping, or distortional, degrees of freedom). The three-dimensional motion of each cross section has five components: two displacements and three rotations (seen in Figure 2-3). If the long dimension of the blade is oriented along the *x*-axis, the displacements of the cross section are in the *y*- and *z*-direction. The three rotations are around each of the coordinate axes. Displacement in the *x*-direction is captured by distortional degrees of freedom, δ, at each node as seen in Figure 2-2.

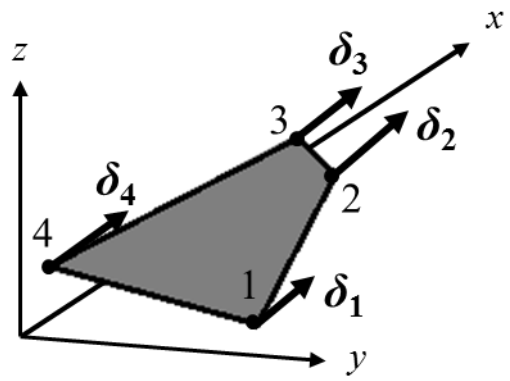

Figure 2-2: Membrane Element with Distortional Degrees of Freedom

The behavior of a typical blade surface element is controlled by the movement of the two cross sections it connects as well as four distortional degrees of freedom, one at each node. When the local numbering of the nodes is assigned as in Figure 2-3, nodes 1 and 4 are on cross section J and nodes 2 and 3 are on cross section K. The elemental vector of degrees of freedom which is made up of 14 degrees of freedom is organized as

$$\mathbf{d}_e^{\mathrm{T}} = \left\{ v_{y\mathrm{J}}, v_{z\mathrm{J}}, \theta_{x\mathrm{J}}, \theta_{y\mathrm{J}}, \theta_{z\mathrm{J}}, v_{y\mathrm{K}}, v_{z\mathrm{K}}, \theta_{x\mathrm{K}}, \theta_{y\mathrm{K}}, \theta_{z\mathrm{K}}, \delta_1, \delta_2, \delta_3, \delta_4 \right\} \tag{2.3}$$

where:

$v_{y\mathrm{J}}$, $v_{y\mathrm{K}}$: displacement of cross section J or K in the *y*-direction

$v_{z\mathrm{J}}$, $v_{z\mathrm{K}}$: displacement of cross section J or K in the *z*-direction

$\theta_{x\mathrm{J}}$, $\theta_{x\mathrm{K}}$: rotation about the *x*-axis at cross section J or K (torsion)

$\theta_{y\mathrm{J}}$, $\theta_{y\mathrm{K}}$: rotation about the *y*-axis at cross section J or K (bending in *xz*-plane)

$\theta_{z\mathrm{J}}$, $\theta_{z\mathrm{K}}$: rotation about the *z*-axis at cross section J or K (bending in *xy*-plane)

δ_{I} : displacement of node I (I = 1,2,3,4) in *x*-direction (warping)

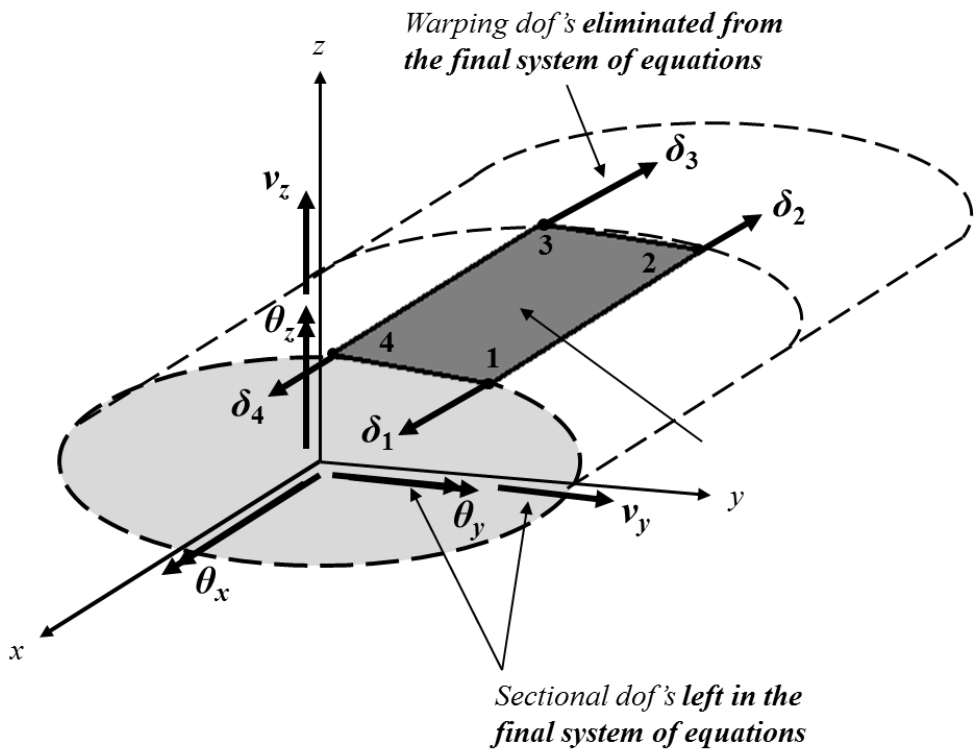

Figure 2-3: Elemental Degrees of Freedom

2.1.3 Internal and External Segments

Oftentimes, wind turbine blades will have an internal web or multiple webs, as shown in **Error! Reference source not found.**. These so-called shear webs, or internal walls, may have material properties that greatly differ from that of the exterior wall. If the shear webs are much stiffer than the rest of the structure, the warping of the cross section will not be smooth and the blade model must accurately capture this behavior.

Figure 2-4: Possible Internal Web Configurations

The thin-walled beam model proposed here is capable of accounting for such internal walls, for abruptly changing material properties and for sharp corners in the cross section, through the use of segments. One logical use of segments is to have one segment be the exterior walls of the blade and another segment as the internal shear web. Each segment could then be assigned its own material property. Additionally, it could be the case that the internal segment terminates at some location along the blade, which can also be easily accounted for in the model utilizing the concept of segments.

The addition of internal segments does not affect the degrees of freedom as explained previously. The internal segment would simply add a number of nodes to the cross section. The wind turbine blade would then have elements on the exterior of the structure, as well as internal elements at the location of the shear web. The displacements of each element is still affected by the translational and rotational degrees of freedom of neighboring cross sections as well as distortional degrees of freedom at the nodes along the exterior wall as well as the nodes along the web.

2.1.4 Outline of Basic Equations

The basic equations used in the thin-walled beam are those of two-dimensional elasticity problems; the difference, specified in Section 2.2 , is in how strains are calculated. To begin, we first consider the weak formulation of the wind turbine blade problem. The finite elements as described in previous sections are used to discretize the system in order to approximate the solution to the problem. Following the procedure described in Section 2.5 the following undamped equation of motion is obtained

$$\mathbf{M}\ddot{\mathbf{d}}(t) + \mathbf{K}\mathbf{d}(t) = \mathbf{f}^{\mathbf{ext}}(t) \tag{2.4}$$

where **M** and **K** are the mass and stiffness matrices, respectively. The external force vector, $\mathbf{f}^{\mathbf{ext}}$, can be prescribed in analysis of structural problems alone, or results from the fluid pressure on the blade at a given timestep, in the fluid-structure interaction analysis. The global displacement vector, **d**, and its second time derivative, $\ddot{\mathbf{d}}$, appear as a result of

the assembly of the elemental contribution to the global equations and is composed of the degrees of freedom given in Eq. ((**2.3**).

The stiffness matrix (for isotropic materials only), given in Eq. ((2.5) below represents the (variation in) elastic strain energy.

$$\boldsymbol{\delta}\mathbf{d}^{\mathrm{T}}\mathbf{K}\mathbf{d} = \int_{\mathrm{V}} \left(\mathrm{E}\boldsymbol{\delta\varepsilon}^{\mathrm{T}}\boldsymbol{\varepsilon} + \mathrm{G}\boldsymbol{\delta\gamma}^{\mathrm{T}}\boldsymbol{\gamma}\right) d\,\mathrm{V} \tag{2.5}$$

where $\boldsymbol{\delta}\mathbf{d}$ is the arbitrary variation of $\mathbf{d}$, $\boldsymbol{\varepsilon}$ is the longitudinal component of strain and $\boldsymbol{\gamma}$ is the shear component of strain in the membrane element; $\boldsymbol{\delta\varepsilon}$, $\boldsymbol{\delta\gamma}$ are their variations. Further discussion of the formation of the stiffness matrix is detailed in Sections 2.2 and 2.3. The kinetic energy of the system comes into play in the mass matrix. The following is the variational form of virtual work done by inertia forces.

$$\boldsymbol{\delta}\mathbf{d}^{\mathrm{T}}\mathbf{M}\ddot{\mathbf{d}} = \int_{\mathrm{V}} \left(\rho\boldsymbol{\delta}\mathbf{u}^{\mathrm{T}}\ddot{\mathbf{u}}\right) d\,\mathrm{V} \tag{2.6}$$

where $\mathbf{u}$ is the displacement vector within the element, $\boldsymbol{\delta}\mathbf{u}$ is its variation, and ρ is mass density. Section 2.5 will discuss how this expression is evaluated for elements of the thin-walled beam. Lastly, the external force vector results from the work done on the system by external forces.

2.2 **Evaluation of Strains**

Strains in the wind turbine blade are due to bending, torsional, and distortional (or warping) degrees of freedom. Invoking the assumption that the cross sections remain rigid in-plane, we are left with two strain components to compute: normal strains, $\boldsymbol{\varepsilon}$, and shear strains, $\boldsymbol{\gamma}$.

The details presented later in this section lead to the following two equations:

$$\boldsymbol{\varepsilon} = \mathbf{B}_{\varepsilon}\mathbf{d}_{e} \tag{2.7}$$

$$\boldsymbol{\gamma} = \mathbf{B}_{\gamma}\mathbf{d}_{e} \tag{2.8}$$

where $\mathbf{B}_{\varepsilon}$ and $\mathbf{B}_{\gamma}$ are strain matrices that relate all degrees of freedom of the element to the respective strains $\boldsymbol{\varepsilon}$ and $\boldsymbol{\gamma}$. Figure 2-5 visually depicts how each type of degree of freedom affects both longitudinal and shear strains.

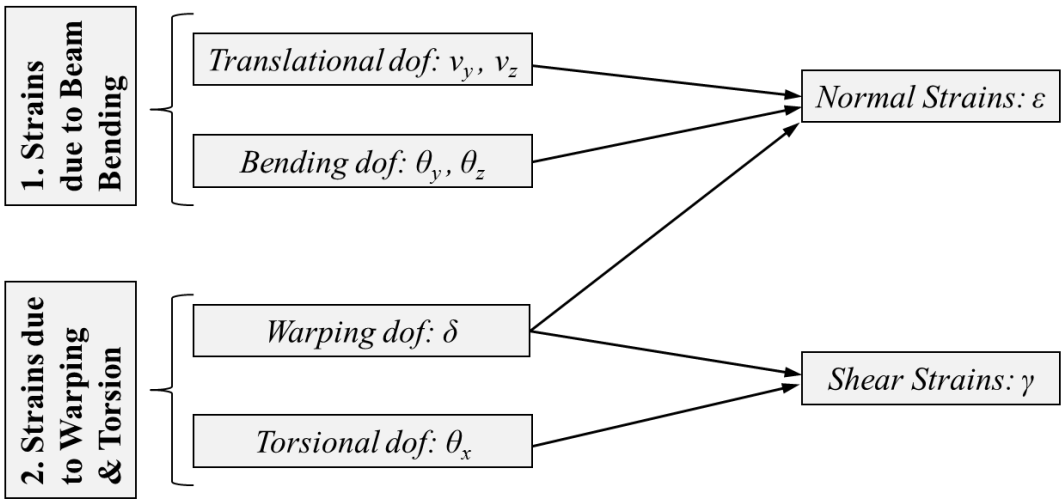

Figure 2-5: Effect of Degrees of Freedom on Strains

As indicated in the second paragraph of Section 2.1.2, $\boldsymbol{\varepsilon}$ and $\boldsymbol{\gamma}$, and thus $\mathbf{B}_{\varepsilon}$ and $\mathbf{B}_{\gamma}$ of Eqs. ((**2.7**) and ((**2.8**), have to be expressed in terms of ξ and η.

2.2.1 Nodal Displacements of Membrane Elements

Consider a typical membrane element like that shown in Figure 2-6. Each node has three displacement components, one component in each of the global coordinate directions.

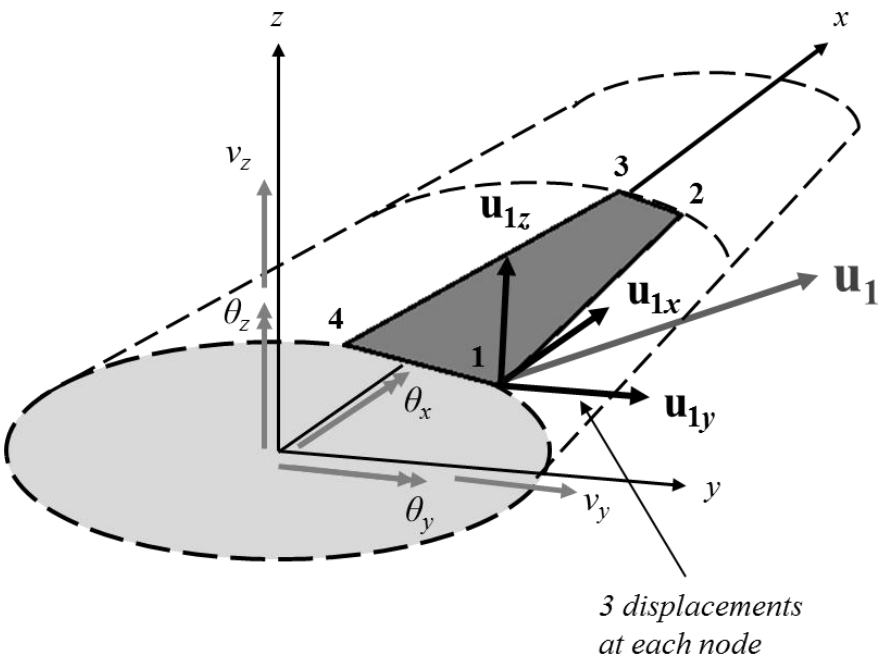

Figure 2-6: Nodal Displacements

As explained previously, the motion of the cross section affects the displacements of each node in that cross section. Specifically, the displacement vector of a single membrane element node is given as:

$$\mathbf{u}_{\mathrm{I}} = \begin{Bmatrix} \mathrm{u}_{\mathrm{I}x} \\ \mathrm{u}_{\mathrm{I}y} \\ \mathrm{u}_{\mathrm{I}z} \end{Bmatrix} = \begin{Bmatrix} -y_{\mathrm{I}}\,\theta_z + z_{\mathrm{I}}\theta_{\mathrm{y}} + \delta_{\mathrm{I}} \\ v_y - z_{\mathrm{I}}\,\theta_x \\ v_z + y_{\mathrm{I}}\theta_x \end{Bmatrix} \tag{2.9}$$

where the degrees of freedom are for the cross section containing node I. The coordinates of the node of interest, *y* and *z*, also appear in the displacement equations.

So, if the cross section translates in the *y*- or *z*-direction, it affects u_y or u_z of the nodes on that cross section. Torsion, represented by θ_x, also affects both u_y and u_z since

the cross section rotates. Bending in the *y*- or *z*-plane, represented by θ_y or θ_z, would result in non-zero *x*-components of the nodal displacements.

Unlike other models, the thin-walled beam model has only two translational degrees of freedom of the cross section, v_y and v_z. Movement in the *x*-direction is captured instead by the distortional degrees of freedom, δ, at each node.

2.2.2 Strains Due to Bending of the Beam

As seen in Figure 2-5, displacement and bending degrees of freedom result in longitudinal strains only. These strains at node I (I = 1,2,3,4), $\bar{\varepsilon}_{\mathrm{I}}$, are computed by simply taking the derivative of the *x*-displacement with respect to *x* ignoring the warping degrees of freedom for now. Following Eq. ((**2.14**), we have

$$\bar{\varepsilon}_{\mathrm{I}} = \frac{\partial \mathrm{u}_{\mathrm{Ix}}}{\partial x} = \frac{\partial\left(-y_{\mathrm{I}}\theta_z + z_{\mathrm{I}}\theta_y\right)}{\partial x} \tag{2.10}$$

and, assuming that

$$\begin{aligned} \theta_z &= \frac{\partial v_y}{\partial x} \\ \theta_y &= -\frac{\partial v_z}{\partial x} \end{aligned} \tag{2.11}$$

the strains at a given node can be written as

$$\bar{\varepsilon}_{\mathrm{I}} = -y_{\mathrm{I}}\frac{\partial^2 v_y}{\partial x^2} + z_{\mathrm{I}}\frac{\partial^2 v_z}{\partial x^2} \tag{2.12}$$

The displacements v_y and v_z can be related to the nodal degrees of freedom using the formulas

$$\begin{aligned} v_y(\bar{x}) &= v_{y\mathrm{J}}\,\overline{\mathrm{N}}_1(\bar{x}) + \theta_{z\mathrm{J}}\,\overline{\mathrm{N}}_2(\bar{x}) + v_{y\mathrm{K}}\,\overline{\mathrm{N}}_3(\bar{x}) + \theta_{z\mathrm{K}}\,\overline{\mathrm{N}}_4(\bar{x}) \\ v_z(\bar{x}) &= v_{z\mathrm{J}}\,\overline{\mathrm{N}}_1(\bar{x}) - \theta_{y\mathrm{J}}\,\overline{\mathrm{N}}_2(\bar{x}) + v_{z\mathrm{K}}\,\overline{\mathrm{N}}_3(\bar{x}) - \theta_{y\mathrm{K}}\,\overline{\mathrm{N}}_4(\bar{x}) \end{aligned} \tag{2.13}$$

where $\overline{\mathrm{N}}_1, \overline{\mathrm{N}}_2, \overline{\mathrm{N}}_3, \overline{\mathrm{N}}_4$ are the usual Hermite shape functions

$$\begin{aligned}\overline{\mathrm{N}}_1(\bar{x}) &= 2\bar{x}^3 - 3\bar{x}^2 + 1 \\ \overline{\mathrm{N}}_2(\bar{x}) &= \mathrm{a}\left(\bar{x}^3 - 2\bar{x}^2 + \bar{x}\right) \\ \overline{\mathrm{N}}_3(\bar{x}) &= -2\bar{x}^3 + 3\bar{x}^2 \\ \overline{\mathrm{N}}_4(\bar{x}) &= \mathrm{a}\left(\bar{x}^3 - \bar{x}^2\right)\end{aligned} \tag{2.14}$$

The variable 'a' that appears in these equations is the element length, or *x*-dimension from cross section J to cross section K, and $\bar{x} = (x - x_{\mathrm{J}})/\mathrm{a}$, $\bar{x} \in [0,1]$. Functions $\overline{\mathrm{N}}_1$ and $\overline{\mathrm{N}}_3$ reduce to either zero or one if the point of interest is located at one of the nodes. Functions $\overline{\mathrm{N}}_2$ and $\overline{\mathrm{N}}_4$ vanish at both elements ends, but their derivatives possess the same properties as functions $\overline{\mathrm{N}}_1$ and $\overline{\mathrm{N}}_3$. Thus, Eq. ((**2.13**) evaluated at the nodes gives either $v_{y\mathrm{J}}$, $v_{z\mathrm{J}}$ or $v_{y\mathrm{K}}$, $v_{z\mathrm{K}}$ whereas derivatives of Eq. ((**2.13**) evaluated at the nodes yield $\theta_{y\mathrm{J}}$, $\theta_{z\mathrm{J}}$ or $\theta_{y\mathrm{K}}$, $\theta_{z\mathrm{K}}$, respectively. If the point of interest is not at a node, some combination of these cross-sectional displacements and rotations, as specified in Eq. ((**2.13**), will approximate the value of the displacements v_y and v_z at that point.

The combination of Eqs. ((**2.12**) through ((**2.14**) yields bending-related strain, $\bar{\varepsilon}_{\mathrm{I}}$ at node I, which is expressed in terms of Cartesian coordinates *x*, *y*, *z*. Since these strains were computed using the Hermite shape functions (of Eq. (2.13)), the bending-related strain can be written with respect to the beam degrees of freedom, $\mathbf{d}_e$, as

$$\bar{\varepsilon}_{\mathrm{I}} = \overline{\mathbf{B}}_{\mathrm{I}}\mathbf{d}_e \tag{2.15}$$

where $\overline{\mathbf{B}}_{\mathrm{I}}$ is the strain matrix due to bending of the beam evaluated at point I, or equivalently,

$$\overline{\mathbf{B}}_{\mathrm{I}} = \overline{\mathbf{B}}_1, \overline{\mathbf{B}}_2, \overline{\mathbf{B}}_3, \overline{\mathbf{B}}_4 \tag{2.16}$$

where $\overline{\mathbf{B}}_1, \overline{\mathbf{B}}_2, \overline{\mathbf{B}}_3, \overline{\mathbf{B}}_4$ contain coordinates of nodes 1, 2, 3, 4, respectively, and derivatives of the functions $\overline{\mathrm{N}}_1, \overline{\mathrm{N}}_2, \overline{\mathrm{N}}_3, \overline{\mathrm{N}}_4$ evaluated at those locations as seen in Eq. (2.17).

$$\begin{aligned}
\overline{\mathbf{B}}_1 &= \frac{1}{a^2}\{-6y_1,-6z_1,0,4az_1,-4ay_1,6y_1,6z_1,0,2az_1,-2ay_1,0,0,0,0\} \\
\overline{\mathbf{B}}_2 &= -\frac{1}{a^2}\{6y_2,6z_2,0,-2az_2,2ay_2,-6y_2,-6z_2,0,-4az_2,4ay_2,0,0,0,0\} \\
\overline{\mathbf{B}}_3 &= -\frac{1}{a^2}\{6y_3,6z_3,0,-2az_3,2ay_3,-6y_3,-6z_3,0,-4az_3,4ay_3,0,0,0,0\} \\
\overline{\mathbf{B}}_4 &= \frac{1}{a^2}\{-6y_4,-6z_4,0,4az_4,-4ay_4,6y_4,6z_4,0,2az_4,-2ay_4,0,0,0,0\}
\end{aligned} \tag{2.17}$$

2.2.3 Strains Due to Distortional and Torsional Degrees of Freedom

The second and final group of degrees of freedom that contribute to strains, as seen in Figure 2-5 contains the torsional degrees of freedom, θ_x, and warping degrees of freedom, δ. While θ_x causes shear stresses only, δ causes both normal and shear strains. The degrees of freedom discussed in the previous section contributed to normal stresses only. So, the total normal strain is the sum of the strains from each contribution.

As explained in Section 2.2.1, nodal displacements are expressed in the global *xyz*-coordinate system. Ultimately then, strains from distortional and torsional degrees of freedom should also be expressed in global coordinates. However, this is not so straightforward with non-prismatic (distorted) elements. The appropriate way to express these strains with non-planar elements is using curvilinear coordinates as is common in continuum mechanics.

The covariant strain components used in this thesis due to torsion and warping are given by

$$\varepsilon_{\alpha\beta} = \frac{1}{2}\left(\mathbf{u}_{,\alpha} \bullet \mathbf{G}_{\beta} + \mathbf{u}_{,\beta} \bullet \mathbf{G}_{\alpha}\right) \tag{2.18}$$

where $\alpha,\beta \in \{1,2\} = \{\xi,\eta\}$, $\mathbf{G}_\alpha$ and $\mathbf{G}_\beta$ are related to the position vector of Eq. ((**2.1**), and $\mathbf{u}_{,\alpha}$ and $\mathbf{u}_{,\beta}$ are derivatives with respect to ξ,η of the displacement vector given by

$$\mathbf{u}(\xi,\eta)=\begin{Bmatrix} u_x(\xi,\eta) \\ u_y(\xi,\eta) \\ u_z(\xi,\eta) \end{Bmatrix}=\begin{Bmatrix} \sum_{I=1}^{4} u_{Ix} N_I(\xi,\eta) \\ \sum_{I=1}^{4} u_{Iy} N_I(\xi,\eta) \\ \sum_{I=1}^{4} u_{Iz} N_I(\xi,\eta) \end{Bmatrix} \tag{2.19}$$

This results in strains due to torsion and warping as a function of nodal displacements u_{1x}, u_{1y}, u_{1z}, etc. To stay consistent with the format of Eq. ((**2.15**), transformation is required so that the strains of Eq. ((**2.18**) are a function of the beam degrees of freedom, $\mathbf{d}_e$. After transformation, and in view of the in-plane rigidity of the cross section imposed in this thesis, normal and shear strains as a result of torsion and warping are given as

$$\begin{aligned} \tilde{\varepsilon}_x &= \tilde{\varepsilon} = \tilde{\mathbf{B}}_{11}\mathbf{d}_e \\ \tilde{\gamma}_{xy} &= \tilde{\gamma} = \tilde{\mathbf{B}}_{12}\mathbf{d}_e \end{aligned} \tag{2.20}$$

where $\tilde{\mathbf{B}}_{11}$ and $\tilde{\mathbf{B}}_{12}$ are the first and the third rows of the strain matrix due to torsion and warping, $\tilde{\mathbf{B}}$. The development of these strains is explained extensively in 0.

2.2.4 Total Strains

The normal and shear strains are the sum of all translational, rotational, and distortional contributions to strain. So, the addition of Eqs. ((**2.15**) and ((**2.20**) gives the total strains due to all degrees of freedom as

$$\begin{aligned} \varepsilon_I = (\bar{\mathbf{B}}_I + (\tilde{\mathbf{B}}_{11})_I)\mathbf{d}_e = (\mathbf{B}_1)_I\mathbf{d}_e \quad , \quad \varepsilon = \sum_{I=1}^{4} \varepsilon_I N_I(\xi,\eta) \\ \gamma = \tilde{\mathbf{B}}_{12}\mathbf{d}_e = \mathbf{B}_2\mathbf{d}_e \end{aligned} \tag{2.21}$$

where $\mathbf{B}_1$ and $\mathbf{B}_2$ are matrices containing all contributions to normal strains and shear strains, respectively.

In the subsequent evaluation of the stiffness matrix, the normal and shear strains must be evaluated at integration points. Those integration points will be defined in terms

of element isoparametric coordinates ξ,η. Thus, the strains needed to be expressed in terms of ξ and η. While warping and torsion-related contributions to strains, i.e.: $\tilde{\mathbf{B}}_{11}$ and $\tilde{\mathbf{B}}_{12}$ of Eq. ((**2.20**), have been defined directly in terms of those coordinates (of Appendix A3), the bending-related strains, i.e. matrix $\bar{\mathbf{B}}$ of Eq. ((**2.21**), have not. To overcome this incompatibility, the procedure described below is followed.

For the calculation of normal strains, the bilinear approximating functions defined previously in Eq. ((**2.2**) are used to describe the normal strain at any point within the element. The final matrix for normal strains, $\mathbf{B}_{\varepsilon}$, is given as

$$\mathbf{B}_{\varepsilon}(\xi,\eta)=\sum_{\mathrm{I}=1}^{4}(\mathbf{B}_{\mathbf{1}})_{\mathrm{I}}\mathrm{N}_{\mathrm{I}}(\xi,\eta) \tag{2.22}$$

where $(\mathbf{B}_{\mathbf{1}})_{\mathrm{I}}$ is the $\mathbf{B}_{\mathbf{1}}$ matrix of Eq. ((**2.21**) evaluated at the nodal point I.

The process for evaluating shear strains is different in that the $\mathbf{B}_{\mathbf{2}}$ matrix is not evaluated at the nodal points. This recognizes the fact that in nearly all cases, such as in the torsion of I-beams for example, warping of cross sections is predominantly the result of in-plane bending of segments forming the cross section. Such bending, and thus warping, may be severely constrained if shear strains are not properly identified. For the bilinear isoparametric formulation adopted in this thesis, one way of modifying shear strains is based on the so-called "reduced integration" or the assumed strain approach [18,19]. The approach used here is related to the reduced integration technique. Thus, $\mathbf{B}_{\mathbf{2}}$ is evaluated at two points, *m* and *n*: $(\xi,\eta)_{m,n}=(0,\pm\frac{\sqrt{3}}{3})$ located in the plane perpendicular to the axis of the beam. This way, no shearing effects will be seen when the warping of an element is the result of its in-plane bending. It should be noted that shear strain is independent of ξ within the element since points *m* and *n* have the same ξ-value. Similar to Eq. ((**2.22**), the final matrix for shear strains, $\mathbf{B}_{\gamma}$, is given by

$$\mathbf{B}_{\gamma}(\xi,\eta)=\sum_{\mathrm{i}=1}^{2}(\mathbf{B}_{\mathbf{2}})_{\mathrm{i}}\hat{\mathrm{N}}_{\mathrm{i}}(\eta) \tag{2.23}$$

where $(\mathbf{B_2})_i$ is the $\mathbf{B_2}$ matrix evaluated at the points *m* and *n*. Since the shear strain is approximated using only two points, the bilinear approximating functions are not used. Instead, the approximating function $\hat{N}$ is used which is given as:

$$\hat{N}_I(\eta) = \left(\frac{1 \pm \eta_I \sqrt{3}}{2} \right) \tag{2.24}$$

So, the final expressions relating strains and displacements are given as

$$\begin{aligned} \boldsymbol{\varepsilon}(\xi,\eta) &= \mathbf{B}_{\varepsilon}(\xi,\eta)\mathbf{d}_e \\ \boldsymbol{\gamma}(\xi,\eta) &= \mathbf{B}_{\gamma}(\xi,\eta)\mathbf{d}_e \end{aligned} \tag{2.25}$$

which contain contributions to normal and shear strains from all degrees of freedom. This relationship will be used for the formation of the stiffness matrix as detailed in the following section.

2.3 **Evaluation of Element Stiffness Matrix**

The equation for the element stiffness matrix, assuming isotropic material properties, results from the following formula representing the virtual work of internal forces

$$\boldsymbol{\delta}\mathbf{d}_e^{\mathrm{T}}\mathbf{K}_e\mathbf{d}_e = \int_{\mathrm{V}} \left(\mathrm{E}\boldsymbol{\delta\varepsilon}^{\mathrm{T}}\boldsymbol{\varepsilon} + \mathrm{G}\boldsymbol{\delta\gamma}^{\mathrm{T}}\boldsymbol{\gamma}\right) d\,\mathrm{V} \tag{2.26}$$

In view of Eq. ((**2.25**), one has

$$\begin{aligned} \boldsymbol{\delta\varepsilon} &= \mathbf{B}_{\varepsilon}(\xi,\eta)\boldsymbol{\delta}\mathbf{d}_e \\ \boldsymbol{\delta\gamma} &= \mathbf{B}_{\gamma}(\xi,\eta)\boldsymbol{\delta}\mathbf{d}_e \end{aligned} \tag{2.27}$$

Thus, Eq. ((2.26) can be re-written in matrix form as follows.

$$\boldsymbol{\delta}\mathbf{d}_e^{\mathrm{T}}\mathbf{K}_e\mathbf{d}_e = \boldsymbol{\delta}\mathbf{d}_e^{\mathrm{T}}\left(\int_{\mathrm{V}} \begin{Bmatrix} \mathbf{B}_{\varepsilon}(\xi,\eta) \\ \mathbf{B}_{\gamma}(\xi,\eta) \end{Bmatrix}^{\mathrm{T}} \begin{bmatrix} \mathrm{E} & 0 \\ 0 & \mathrm{G} \end{bmatrix} \begin{Bmatrix} \mathbf{B}_{\varepsilon}(\xi,\eta) \\ \mathbf{B}_{\gamma}(\xi,\eta) \end{Bmatrix} d\,\mathrm{V}\right)\mathbf{d}_e \tag{2.28}$$

Introducing the following matrices

$$\begin{aligned} \mathbf{B} &\equiv \begin{Bmatrix} \mathbf{B}_{\varepsilon}(\xi,\eta) \\ \mathbf{B}_{\gamma}(\xi,\eta) \end{Bmatrix} \\ \mathbf{D} &\equiv \begin{bmatrix} \mathrm{E} & 0 \\ 0 & \mathrm{G} \end{bmatrix} \end{aligned} \tag{2.29}$$

and recognizing that for thin-walled membrane elements, the elemental volume is the product of area and local element thickness

$$\mathrm{t}(\xi,\eta) = \sum_{\mathrm{I}=1}^{4} \mathrm{t}_{\mathrm{I}}\mathrm{N}_{\mathrm{I}}(\xi,\eta) \tag{2.30}$$

where t_{I} is the thickness of the element at node I. The formula for the element stiffness matrix, $\mathbf{K}_e$, then takes the form

$$\mathbf{K}_e = \int_{\mathrm{A}} \mathbf{B}^{\mathrm{T}}(\xi,\eta)\mathbf{D}\mathbf{B}(\xi,\eta)\mathrm{t}(\xi,\eta)\,J(\xi,\eta)\,d\,\mathrm{A} = \int_{-1}^{1}\int_{-1}^{1} \mathbf{B}^{\mathrm{T}}(\xi,\eta)\mathbf{D}\mathbf{B}(\xi,\eta)\mathrm{t}(\xi,\eta)\,J(\xi,\eta)\,d\,\xi\,d\,\eta \tag{2.31}$$

where $J(\xi,\eta)$ is the Jacobian (of Appendix A, Eq. ((A.**11**)) that comes out of the formulation of the strains due to warping and torsion. Gaussian numerical integration is then chosen as the appropriate way to evaluate the integral, which involves the evaluation of the integrand at a number of the so-called Gauss points, (ξ_P,η_Q).

$$\mathbf{K}_e = \sum_P \sum_Q w_P w_Q \left(\mathbf{B}^T \mathbf{D} \mathbf{B} t J\right)\Big|_{\xi_P \eta_Q} \tag{2.32}$$

where w_P and w_Q are weighting coefficients associated with the Gauss points. Two Gauss points in both the ξ and η direction are chosen because for mildly distorted elements, the expression for the stiffness matrix is dominated by biquadratic polynomials with respect to ξ,η.

2.3.1 Supplemental Torsional Stiffness

The stiffness matrix defined by Eq. ((2.32) is based on the assumption that all stresses are constant across the thickness of the structure's wall. The linear variation of the shear stresses across the thickness that always accompanies torsional deformation is neglected. For closed cross sections, the contribution of that linear variation is negligible and the formula presented in Eq. ((2.32) is adequate. For open cross sections, the linear distribution of the shear stresses across the wall of the structure is dominant and has to be included in the stiffness. This additional term is the well understood Saint Venant stiffness and has the following form [17]

$$C = G \sum_{i=1}^{n} \tfrac{1}{3} b_i t_i^3 \tag{2.33}$$

where C is the torsional rigidity of the cross section, b_i is the width of the i^{th} segment the cross section is composed of, t_i is its thickness, and n is the total number of segments in the cross section.

In the finite element formulation presented herein, the additional torsional stiffness is added at the element level. It is related only to the torsional degrees of freedom $\theta_{x\mathrm{J}}$, $\theta_{x\mathrm{K}}$ of that element and has the form

$$\begin{Bmatrix} M_{xJ} \\ M_{xK} \end{Bmatrix} = \frac{C_{ave}}{a} \begin{bmatrix} 1 & -1 \\ -1 & 1 \end{bmatrix} \begin{Bmatrix} \theta_{xJ} \\ \theta_{xK} \end{Bmatrix} \tag{2.34}$$

where $C_{ave} = (C_J + C_K)/2$ and a is the element dimension defined previously.

2.3.2 Anisotropy Considerations

For the calculation of the element stiffness matrix, the matrix **D** contains information about the mechanical properties of the material. In the isotropic case as seen in Eq. ((2.29), there are only two independent elastic constants: E, the modulus of elasticity, and G, the shear modulus. The off-diagonal terms of the **D** matrix are zero, indicating that there is no coupling between normal and shear deformations.

For anisotropic materials, the only thing that changes in the calculation of the stiffness matrix is the **D** matrix. The off-diagonal terms are no longer zero in this case, because there is indeed coupling between normal and shear deformations. Special anisotropic materials called "orthotropic" are often of particular interest. In the two-dimensional case, relevant to thin-walled structures, such materials have four independent elastic constants: Young's moduli, E_1 and E_2, Poisson ratio, ν_1, and the shear modulus as before, G. Orientations 1 and 2 are the principal directions of the material.

There are two steps involved in forming the **D** matrix for anisotropic materials when none of the principal directions of orthotropy coincide with the axis of the beam. First, we form a matrix that relates stress and strain in the principal material directions. Second is the transformation of this matrix into the element's local coordinate system. Since we considered the cross sections of the blade rigid in-plane, **D** is a 2x2 matrix defined as follows [20]

$$\mathbf{D} = \begin{bmatrix} D_{11} & D_{16} \\ D_{16} & D_{66} \end{bmatrix} \tag{2.35}$$

where

$$\begin{aligned} D_{11} &= \overline{D}_{11} cos^4\alpha + \overline{D}_{22} sin^4\alpha + 2\left(\overline{D}_{12} + 2\overline{D}_{66}\right) sin^2\alpha \cos^2\alpha \\ D_{16} &= \left(\overline{D}_{11} - \overline{D}_{12} - 2\overline{D}_{66}\right) cos^3\alpha \sin\alpha - \left(\overline{D}_{22} - \overline{D}_{12} - 2\overline{D}_{66}\right) cos\alpha \sin^3\alpha \\ D_{11} &= \left(\overline{D}_{11} - \overline{D}_{12} - 2\overline{D}_{66}\right) cos\alpha \sin^3\alpha - \left(\overline{D}_{22} - \overline{D}_{12} - 2\overline{D}_{66}\right) cos^3\alpha \sin\alpha \end{aligned} \tag{2.36}$$

where α is the angle between the principal material coordinate system and the element's local coordinate system. Eq. ((2.36) contains entries from a $\overline{\mathbf{D}}$ matrix, which is the matrix for stress-strain relations in the material's principal coordinates. As seen in the following equation [20], these entries of $\overline{\mathbf{D}}$ contain the four independent elastic constants.

$$\begin{aligned}
\overline{D}_{11} &= \frac{E_1}{1-\nu_1^2\frac{E_2}{E_1}} \\
\overline{D}_{22} &= \frac{E_2}{1-\nu_1^2\frac{E_2}{E_1}} \\
\overline{D}_{12} &= \frac{\nu_1 E_2}{1-\nu_1^2\frac{E_2}{E_1}} \\
\overline{D}_{66} &= G
\end{aligned} \tag{2.37}$$

In conclusion, substitution of the new **D** matrix from Eqs. ((2.35) and ((2.32) gives the appropriate expression for the stiffness matrix with elements of anisotropic material properties. In addition to having flexibility for anisotropic materials in the thin-walled beam model, the material properties of each element may also differ. This is especially useful in applications such as wind turbine blades where there may be different types of materials in different segments of the blade. For instance, in Figure 2-4 we saw that there may be internal ribs in addition to the blade walls. Oftentimes, this internal segment will have significantly stiffer material so that the blade essentially acts as an I-beam.

2.4 **Assembly and System Reduction**

To capture the motion of the blade as a whole, the global stiffness matrix must be formed by assembly of the element stiffness matrices. In view of the way a discrete model of the beam is described in this work, this involves a series of loops which, for clarity, are shown in the following flow chart.

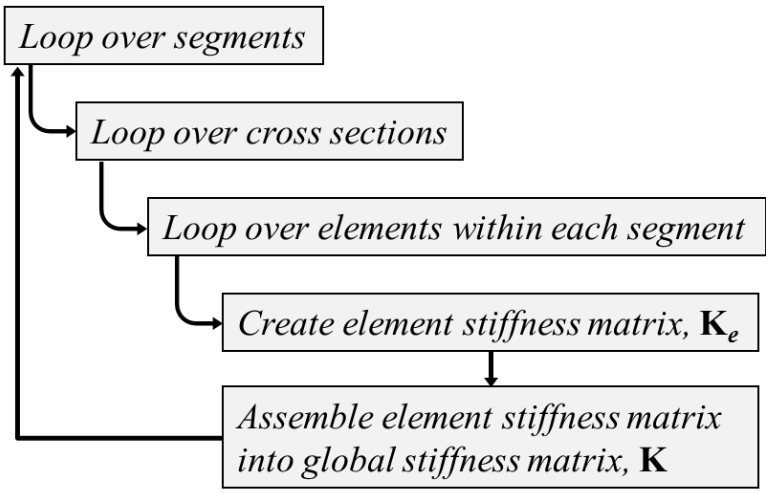

Figure 2-7: Finite Element Analysis Flow Chart

The chosen organization of the global stiffness matrix is such that the cross-sectional degrees of freedom are separated from the distortional degrees of freedom, so that the distortional degrees of freedom can be easily eliminated from the final system of equations. Figure 2-8 illustrates the reduction process for the static system.

$$\mathbf{Kd} = \mathbf{f}^{\mathbf{ext}}$$

$$\begin{bmatrix} \mathbf{K_{dd}} & \mathbf{K_{d\delta}} \\ \mathbf{K_{\delta d}} & \mathbf{K_{\delta\delta}} \end{bmatrix} \{\mathbf{d}\} = \{\mathbf{f}^{\mathbf{ext}}\} = \begin{Bmatrix} \mathbf{f}_{\mathbf{eff}}^{\mathbf{ext}} \\ \mathbf{0} \end{Bmatrix}$$

$$\mathbf{K_{eff}d} = \mathbf{f}_{\mathbf{eff}}^{\mathbf{ext}}$$

Figure 2-8: Static System Reduction

where **d** is the global displacement vector and is given by

$$\mathbf{d}^{\mathrm{T}} = \{v_{y1}, v_{z1}, \theta_{x1}, \theta_{y1}, \theta_{z1}, v_{y2}, v_{z2}, \theta_{x2}, \theta_{y2}, \theta_{z2}, \ldots, v_{yn}, v_{zn}, \theta_{xn}, \theta_{yn}, \theta_{zn}, \delta_{11}, \ldots, \delta_{mn}\} \quad (2.38)$$

with v_{y1} being the displacement of cross section 1 in the *y*-direction, v_{yn} the displacement of the last cross section in the *y*-direction, and so on. The distortional degrees of freedom, or δ's, are arranged by cross section with 'm' representing the number of nodes per cross section. The total number of degrees of freedom is five times larger than the number of cross sections, in addition to the warping degrees of freedom that equals the total number of nodes in all cross sections.

Guyan Reduction (static condensation) is used to reduce out the distortional degrees of freedom and form an effective stiffness matrix, $\mathbf{K}_{\mathbf{eff}}$, calculated as [21]

$$\mathbf{K}_{\mathbf{eff}} = \mathbf{K}_{\mathbf{dd}} - \mathbf{K}_{\delta\mathbf{d}}^{\mathrm{T}} \mathbf{K}_{\delta\delta}^{-1} \mathbf{K}_{\delta\mathbf{d}} \quad (2.39)$$

where $\mathbf{K}_{\mathbf{eff}}$ is a square matrix of size five times greater than the number of cross sections. The corresponding vector of degrees of freedom is then

$$\mathbf{d}^{\mathrm{T}} = \{v_{y1}, v_{z1}, \theta_{x1}, \theta_{y1}, \theta_{z1}, v_{y2}, v_{z2}, \theta_{x2}, \theta_{y2}, \theta_{z2}, \ldots, v_{yn}, v_{zn}, \theta_{xn}, \theta_{yn}, \theta_{zn}\} \quad (2.40)$$

after all of the warping degrees of freedom are eliminated from the system of equations.

This process essentially reduces the size of the system for faster computation time, while not compromising accuracy since the effects of the distortional degrees of freedom are captured in the effective stiffness matrix. This process only works because no external forces associated with warping are applied. The external force vector associated with the reduced (effective) system is $\mathbf{f}_{\mathbf{eff}}^{\mathbf{ext}}$ as seen in Figure 2-8. After completion of the reduction process, the boundary conditions can then be applied, which is the last step before solving the system of equations.

2.5 **Evaluation of Element Mass Matrix**

Formation of the element mass matrix is necessary for the solution to dynamic problems, which is the ultimate goal of this thesis. The dynamic system to be solved in this case is the equation of motion given in Eq. ((2.4). The weak form of the virtual work done by inertia forces has the form

$$\boldsymbol{\delta}\mathbf{d}_e^{\mathrm{T}}\mathbf{M}_e\mathbf{d}_e = \int_{\mathrm{V}} \left(\rho\boldsymbol{\delta}\mathbf{u}^{\mathrm{T}}\ddot{\mathbf{u}}\right) d\,\mathrm{V} \tag{2.41}$$

where ρ is the mean mass density of the element, $\ddot{\mathbf{u}}$ is the second time derivative of the displacement vector. Like the integral for the stiffness term, this volume integral can be turned into an area integral involving the local thickness. This results in the presence of a mass per unit area term, μ, instead of mass per unit volume.

Like nodal displacements, nodal accelerations can be expressed as

$$\ddot{\mathbf{u}}(\xi,\eta) = \begin{Bmatrix} \ddot{\mathbf{u}}_x(\xi,\eta) \\ \ddot{\mathbf{u}}_y(\xi,\eta) \\ \ddot{\mathbf{u}}_z(\xi,\eta) \end{Bmatrix} = \begin{Bmatrix} \sum_{\mathrm{I}=1}^{4} \ddot{\mathrm{u}}_{x\mathrm{I}}\mathrm{N}_{\mathrm{I}}(\xi,\eta) \\ \sum_{\mathrm{I}=1}^{4} \ddot{\mathrm{u}}_{y\mathrm{I}}\mathrm{N}_{\mathrm{I}}(\xi,\eta) \\ \sum_{\mathrm{I}=1}^{4} \ddot{\mathrm{u}}_{z\mathrm{I}}\mathrm{N}_{\mathrm{I}}(\xi,\eta) \end{Bmatrix} \tag{2.42}$$

For convenience, define a new matrix, **H**, as

$$\mathbf{H}_{\mathbf{3x12}} = \left\{\mathrm{N}_1(\xi,\eta)\mathbf{I}_{\mathbf{3x3}}, \mathrm{N}_2(\xi,\eta)\mathbf{I}_{\mathbf{3x3}}, \mathrm{N}_3(\xi,\eta)\mathbf{I}_{\mathbf{3x3}}, \mathrm{N}_4(\xi,\eta)\mathbf{I}_{\mathbf{3x3}}\right\} \tag{2.43}$$

where $\mathbf{I}_{\mathbf{3x3}}$ is a 3x3 identity matrix and N_1, N_2, etc. are N_{I}, approximating functions associated with node I = 1,2,3,4. The element mass matrix, $\hat{\mathbf{M}}_e$, is then computed from Eq. ((2.41) as

$$\hat{\mathbf{M}}_e = \int_{-1}^{1}\int_{-1}^{1} \mu(\xi,\eta)\mathbf{H}^{\mathrm{T}}(\xi,\eta)\mathbf{H}(\xi,\eta)\, J\,(\xi,\eta)\, d\,\xi\, d\,\eta \tag{2.44}$$

The size of this matrix is only 12 by 12 since it is based on the nodal displacements, **u**, instead of the desired degrees of freedom, $\mathbf{d}_e$. This matrix is then transformed further by

using the same transformation matrix (Eq. ((A.**23**) of Appendix A) used to develop the element stiffness matrix.

$$\mathbf{M}_e = \mathbf{T}^{\mathrm{T}} \hat{\mathbf{M}}_e \mathbf{T} \tag{2.45}$$

where $\mathbf{M}_e$ is the 14 by 14 element mass matrix associated with the elemental degrees of freedom.

In the same fashion as the stiffness matrix, the element mass matrices are assembled in order to form the global mass matrix, **M**.

$$\mathbf{M} = \begin{bmatrix} \mathbf{M}_{\mathbf{dd}} & \mathbf{M}_{\mathbf{d}\delta} \\ \mathbf{M}_{\delta\mathbf{d}} & \mathbf{M}_{\delta\delta} \end{bmatrix} \tag{2.46}$$

In order to solve the dynamic equation of motion, the mass matrix is then reduced to the same order as the effective stiffness matrix. In this process the effects of the warping degrees of freedom on the inertia term are neglected, i.e. it is assumed that $\mathbf{M}_{\mathbf{d}\delta} = \mathbf{M}_{\delta\mathbf{d}} = \mathbf{M}_{\delta\delta} = \mathbf{0}$. Thus, the effective mass matrix, $\mathbf{M}_{\mathbf{eff}}$, can be taken equal to $\mathbf{M}_{\mathbf{dd}}$ so that $\mathbf{M}_{\mathbf{eff}}$ is a square matrix of size 5 times larger than the number of cross sections.

2.5.1 Dynamic Equation of Motion

The final system of equations after system reduction and application of boundary conditions is

$$\mathbf{M}_{\mathbf{eff}} \ddot{\mathbf{d}}(t) + \mathbf{K}_{\mathbf{eff}} \mathbf{d}(t) = \mathbf{f}_{\mathbf{eff}}^{\mathbf{ext}}(t) \tag{2.47}$$

where **d** is the global displacement vector of Eq. ((**2.40**) and its second derivative, $\ddot{\mathbf{d}}$.

In the subsequent part of this thesis, the subscript "**eff**" will be omitted, and the effective mass and stiffness matrices will be simply denoted by **M** and **K**. Similarly, the (reduced) external force vector will be denoted by $\mathbf{f}^{\mathbf{ext}}$ from this point on.

2.5.2 Time Integration of Transient Problems

A numerical integration scheme known as the Newmark-β Method was used for the solution of the dynamic system. The method is based on the following two assumptions [21]

$$\begin{aligned} \dot{\mathbf{d}}_{n+1} &= \dot{\mathbf{d}}_n + \left[(1-\gamma)\ddot{\mathbf{d}}_n + \gamma\ddot{\mathbf{d}}_{n+1}\right]\Delta t \\ \mathbf{d}_{n+1} &= \mathbf{d}_n + \dot{\mathbf{d}}_n \Delta t + \left[(1-2\beta)\ddot{\mathbf{d}}_n + 2\beta\ddot{\mathbf{d}}_{n+1}\right]\frac{\Delta t^2}{2} \end{aligned} \tag{2.48}$$

where $\mathbf{d}_{n+1}$ is the displacement vector, $\dot{\mathbf{d}}_{n+1}$ the first derivative, and $\ddot{\mathbf{d}}_{n+1}$ the second derivative or acceleration at time $t_{n+1} = (n+1)\Delta t$. The parameters γ and β were chosen as ½ and ¼, respectively, which correspond to the Constant Average Acceleration Method. This is an unconditionally stable case of the algorithm, and the timestep for the iterative process, Δt, was selected as 0.001 second with a total duration of 2 seconds. In combination with the equation of motion,

$$\mathbf{M}\ddot{\mathbf{d}}_{n+1} + \mathbf{K}\mathbf{d}_{n+1} = \mathbf{f}^{\mathbf{ext}}_{n+1} \equiv \mathbf{f}^{\mathbf{ext}}(t_{n+1}) \tag{2.49}$$

Eq. ((2.48) can be used to numerically approximate $\mathbf{d}_{n+1}$, $\dot{\mathbf{d}}_{n+1}$ when $\mathbf{d}_n$ and $\dot{\mathbf{d}}_{n+1}$ for the previous timestep is known.

CHAPTER 3. MODEL VERIFICATION

3.1 Static Verification Examples

In this section, the results of static tests performed on three different beams: a twisted beam with thin-walled rectangular cross section, a prismatic I-beam, and an elliptical beam with varying cross sections are presented. The goal of the tests was to compare the response of the beams under static loading, in bending and torsion, to known analytical solutions. Further studies involving dynamic systems are discussed later in Section 3.2. MATLAB was used to analyze both the static and dynamic numerical examples.

3.1.1 Formation of the External Force Vector for Static Cases

For the static case, the (reduced) system of equations (of Figure 2-8) is given as

$$\mathbf{K}\mathbf{d}(t) = \mathbf{f}^{\mathbf{ext}}(t) \tag{3.1}$$

This linear system was solved in MATLAB through simple inversion of the effective stiffness matrix. Only concentrated nodal forces were considered in this section, thus, the external force vector contains entries that correspond to the global degrees of freedom associated with the given concentrated force. For example, if a point load is applied at the tip of the beam in the *y*-direction, the magnitude of the load would be entered in the fifth to last row of $\mathbf{f}^{\mathbf{ext}}$ since v_y is the first of five degrees of freedom of the set related to each cross section and as seen in Eq. ((**2.38**). A similar procedure can be used for the application of a torsional moment, for example, as in the case of the I-beam test in Section 3.1.3. The corresponding degree of freedom in this case is the third in the set of five for each cross section (Eq. ((**2.38**)).

3.1.2 Bending Verification

In the following example, a twisted beam with thin-walled rectangular cross section was tested in bending through application of a tip point load. The undeformed

beam was twisted a total of 90 degrees over 140 meters, the total length of the beam. The cross section was 4 meters by 12 meters with a wall thickness of 0.2 meters. The discretization consisted of 20 nodes at each cross section, and 15 cross sections. Lastly, the Young's modulus was chosen as 70 GPa, with 100 MN applied tip loading in the positive *y*-direction.

The deformed and undeformed shapes are shown in Figure 3-1 below. Looking along the *x*-axis (the axis of the beam), Figure 3-2 gives another view of the deflected shape. Due to the twisted original configuration of the beam, the beam experienced displacement in both *y*- and *z*-directions, seen clearly in Figure 3-2, despite being loaded purely in the *y*-direction.

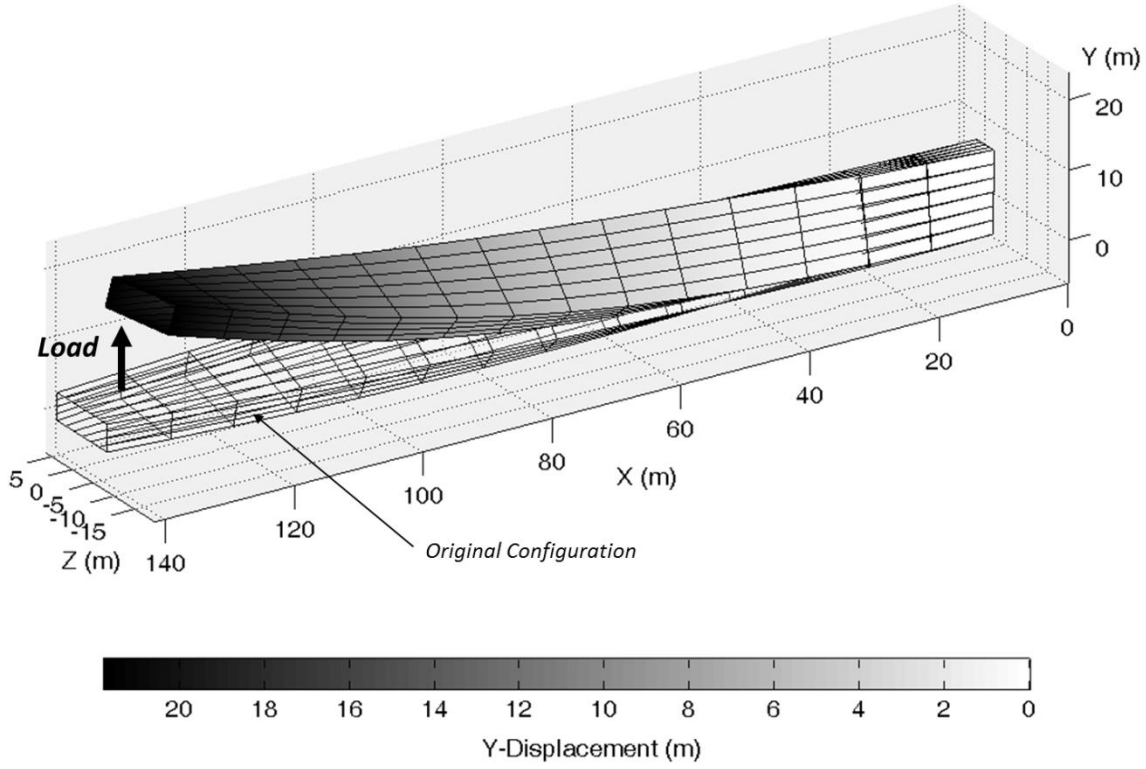

Figure 3-1: Bending of Twisted Beam

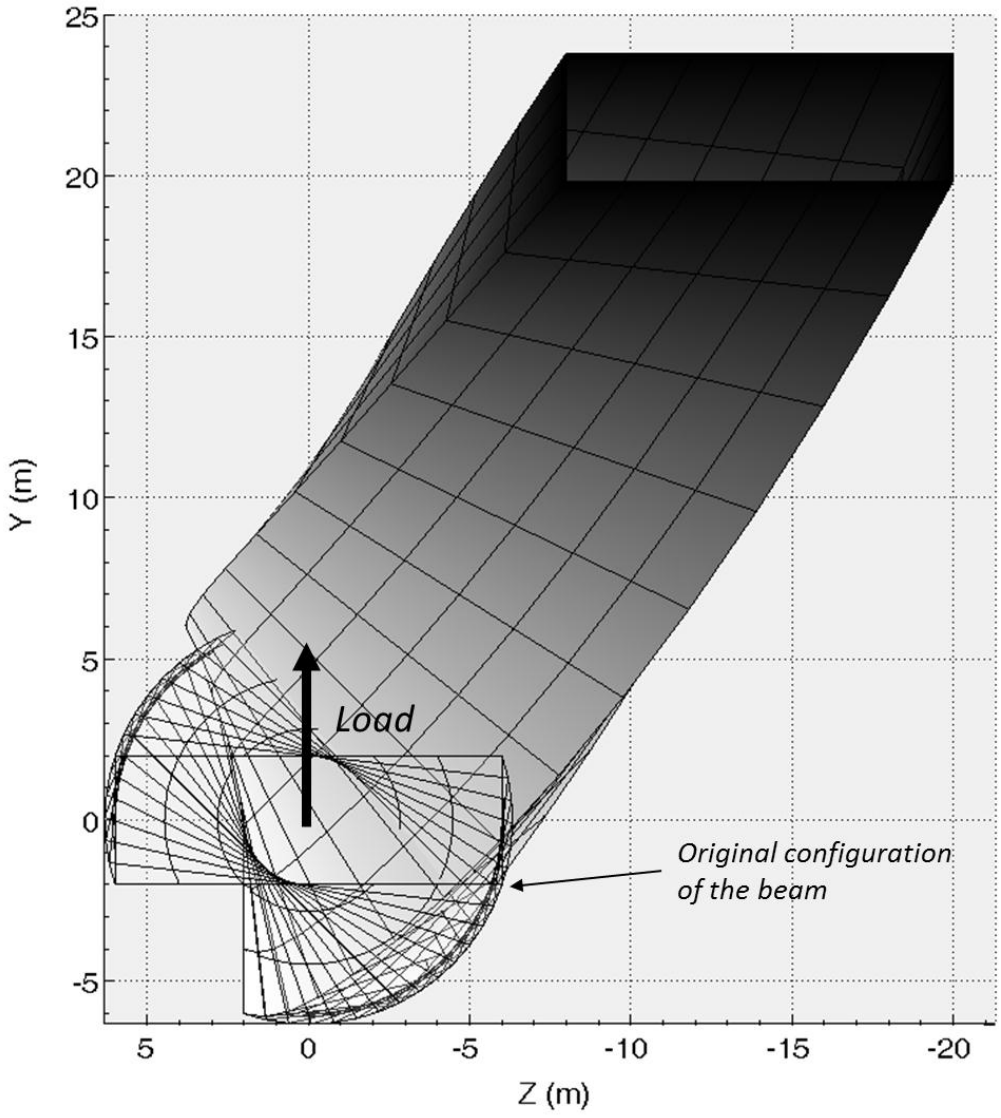

Figure 3-2: Original and Deformed Configuration of Twisted Beam

The analytical solutions for this problem specifying tip displacements due to an external force in the *y*-direction, P_y, can be easily obtained using the theory of asymmetric bending of beams [17] and are given by

$$v_y = \frac{P_y L^3}{6\pi^2 E}\left(\frac{\pi^2+6}{I_z}+\frac{\pi^2-6}{I_y}\right) \tag{3.2}$$

and

$$v_z = \frac{P_y\left(\pi^2 - 4\right)L^3}{2\pi^2 E}\left(\frac{1}{I_z} - \frac{1}{I_y}\right) \tag{3.3}$$

where v_y and v_z are the tip displacements in the *y*- and *z*-directions respectively. These formulas have been developed for beams with solid (compact) cross sections and they do not account for warping. The second moments of inertia, I_y and I_z, also appear in these equations along with the beam length, L. A comparison of the analytical versus numerical results for tip displacements is given in Table 3-1.

Table 3-1: Comparison of Displacements with $P_y = 1x10^8$ N

	Theoretical	Numerical: Thin-Walled Beam Model	Percent Difference (%)
v_y (m)	21.104	21.798	3.233
v_z (m)	-14.147	-13.980	1.184

From these results (in Table 3-1), it is seen that the percent differences between the theoretical and numerical results were as low as 3.233 and 1.184 percent for *y*- and *z*-displacements, respectively. This indicates that the thin-walled beam model is accurately capturing the stiffness of the beam, even with a relatively coarse mesh.

3.1.3 Torsion Verification

As mentioned previously, beam models not accounting for warping cannot accurately capture the behavior of thin-walled beams in torsion. Torsional tests were thus conducted on a prismatic I-beam to see if the thin-walled beam model performed better than standard beam models. The Saint Venant torsional stiffness factor (of Section 2.3.1) was included in this analysis to account for the reduced stiffness of the open cross section. The overall dimensions of the I-beam were selected as 8 meters by 8 meters by 100 meters with a constant wall thickness of 0.05 meter, and Young's modulus of 70 GPa. A torsional moment of 10 MN-m was applied to the tip of the beam; the resulting shape as seen looking along the beam's axis is shown in Figure 3-3. A bottom view of

the deformed shape can be seen in Figure 3-4, where the bottom flange is shown in white and the top flange is black.

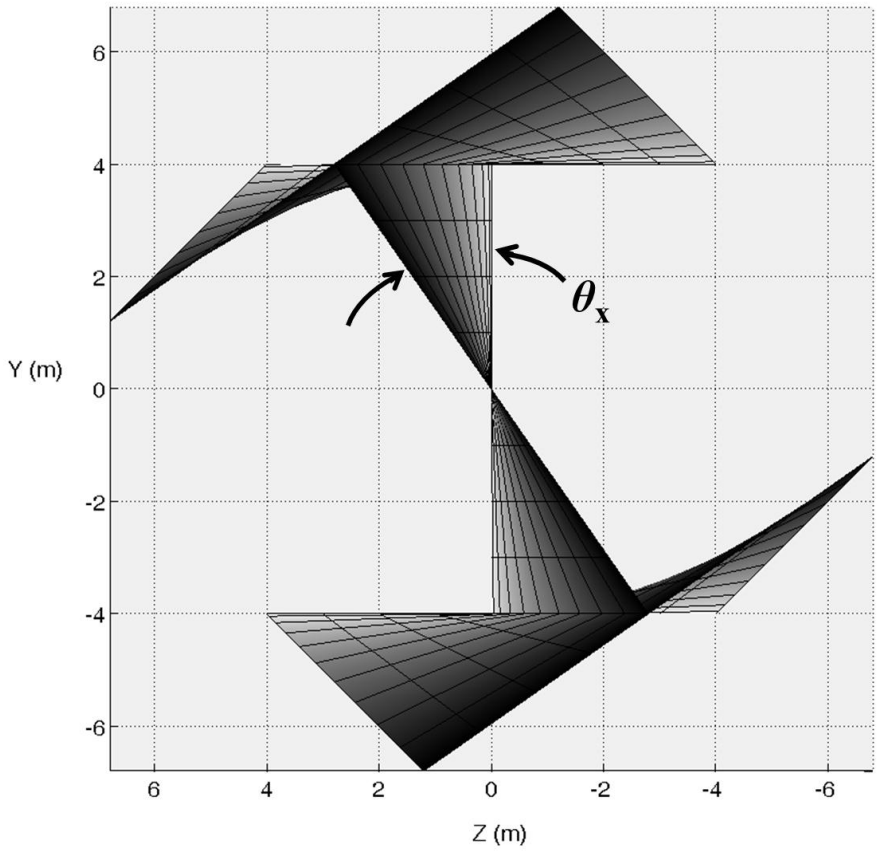

Figure 3-3: I-Beam in Torsion – View Along the Axis

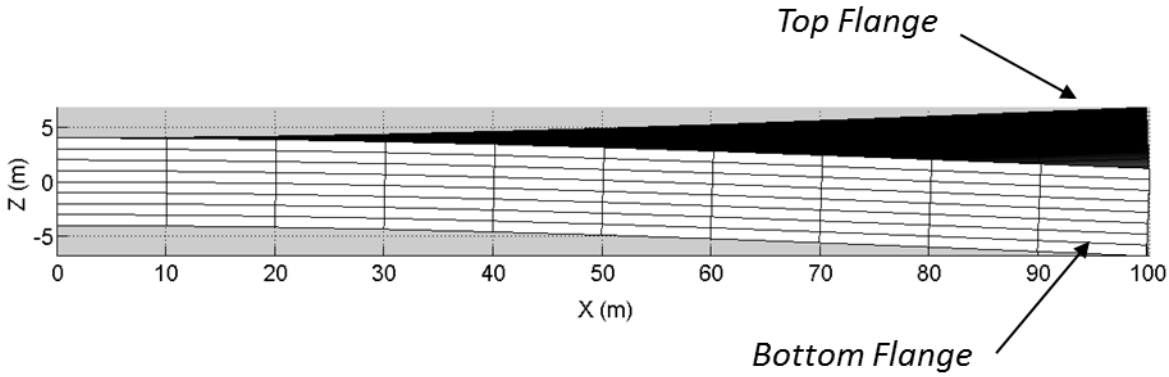

Figure 3-4: I-Beam in Torsion – Bottom View

The total resulting rotation, θ_x, using the thin-walled beam model was 0.6845 radians. The applied torsional moment is equivalently a force couple applied to the flanges of the I-beam with the moment arm as the height of the web. Theoretically, the tip rotation, θ_x, is the displacement of one flange in the beam's transverse direction divided by half of the height of the web. Lastly, the displacement of one flange is $PL^3 / 3EI_f$ from beam theory. Putting this all together, beam theory gives a value of 0.6975 radians for θ_x, which is less than two percent different than that obtained using the thin-walled beam model. 0 contains the detailed calculations for this example.

3.1.4 Variable Cross Section Verification

Wind turbine blades are clearly non-prismatic, with cross sections of varying airfoils along the length to circular cross sections at the blade's hub. So, for illustration purposes, the following example involves two beams with varying cross sections. The first test considered a beam that was circular at the fixed end and tapered off to an ovular cross section at the tip, with the radius of the cross section reduced by some fraction of the circular radius at every cross section, in both *y*- and *z*-directions. The second test maintained the same cross-sectional shapes as the first test but also considered a shift in the beam's axis, another trait that is shared by wind turbine blades. Views along the *x*-axis of both beams are showed in Figure 3-5 and Figure 3-6, with the darker contours indicate the cross sections nearest the tip. Figure 3-7 shows a long view of the (undeformed) beam with varying cross section and shifted axis.

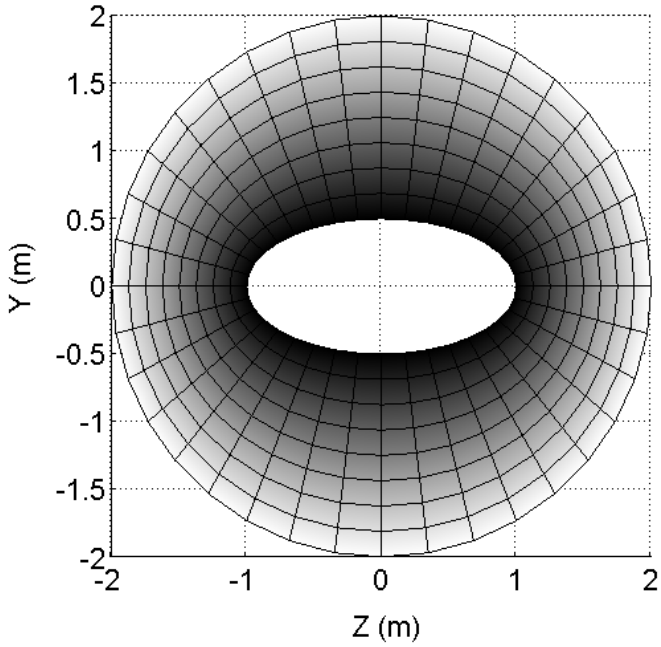

Figure 3-5: Variable Cross Section Beam without Axis Shift

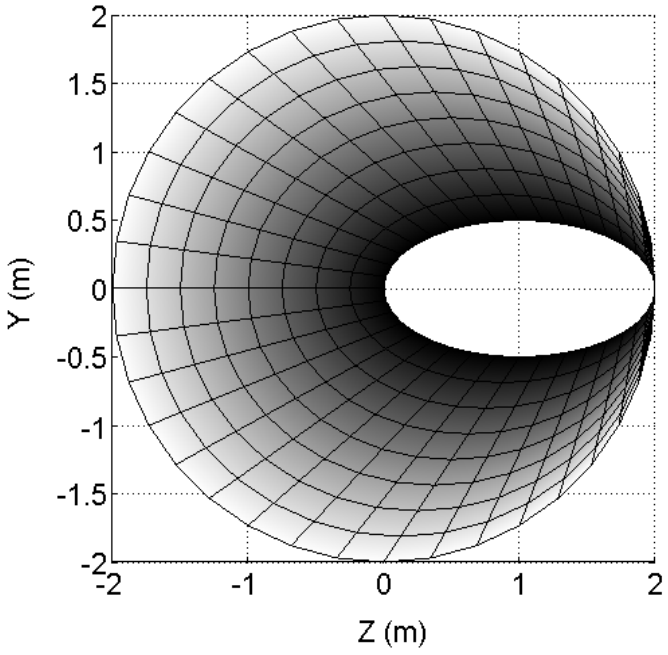

Figure 3-6: Variable Cross Section Beam with Axis Shift

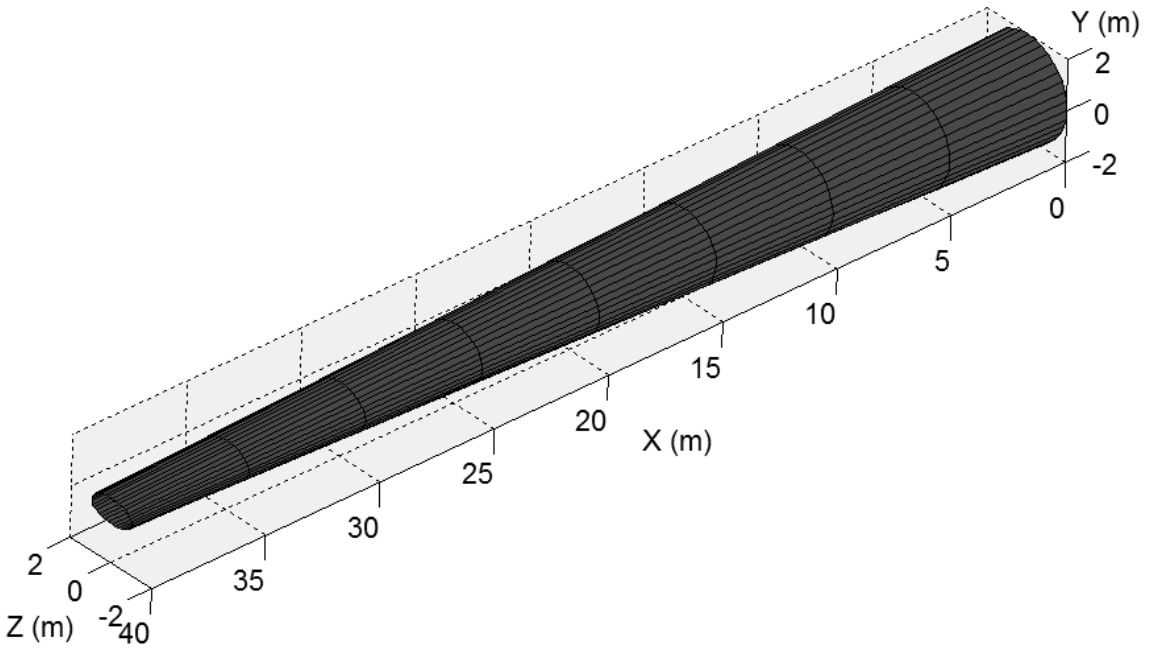

Figure 3-7: Variable Cross Section Beam with Axis Shift – Long View

Similar to previous examples, the material properties for both beams were taken as 70 GPa for Young's Modulus and Poisson ratio of 0.35. The beam length was 100 meters, with the discretization seen clearly in Figures 3-5 and 3-6. Both tests considered loading in the *y*-direction of P_y = 100 MN applied at the center of the tip cross section. The results for both tests for tip displacements and rotations are given in Table 3-2. It can be seen that unlike Test 1, in Test 2 with a shifted beam axis, some torsion (0.060 radians) resulted over the length of the beam. Additionally, the magnitude of the tip displacement increased from 13.814 to 13.869 meters, attributable to the effects of twist about the *x*-axis present in Test 2 thus affecting the tip displacement.

Table 3-2: Effects of Axis Shift on Torsional Rotation

	Test 1: No Axis Shift	Test 2: Axis Shift
v_y (m)	13.814	13.869
θ_x (rad)	0.000	0.060

3.2 **Dynamic Verification Examples**

3.2.1 Free Vibration

The first few modes of vibration will likely be decisive in full fluid-structure interaction, which is the ultimate goal of the thin-walled beam model when applied to wind turbine blades. The first four modes are studied in the following section for verification of the thin-walled beam model.

Recall the (reduced) dynamic equation of motion for free vibration is given as

$$\mathbf{M}\ddot{\mathbf{d}}(t) + \mathbf{K}\mathbf{d}(t) = \mathbf{0} \tag{3.4}$$

Since the system is assumed to be undamped, the natural frequencies are found by solving an eigenvalue problem, $\mathbf{K}\boldsymbol{\varphi} = \omega^2\mathbf{M}\boldsymbol{\varphi}$, with the characteristic equation [21]:

$$\left|\mathbf{K} - \omega_i^2\mathbf{M}\right| = 0 \tag{3.5}$$

where ω_i are the eigenvalues (natural frequencies), $\boldsymbol{\varphi}$ are the related eigenvectors that describe the mode shapes, and $|\cdot|$ represents the determinant.

The MATLAB results for the thin-walled beam finite element model are given in Table 3-3 based on a cylindrical beam of elliptical cross section with cantilever boundary conditions. The dimension of the beam was chosen as 0.2 x 1.0 x 10 meters in length with a wall thickness of 0.02 meter. Young's modulus and Poisson's ratio were 70 GPa and 0.35, respectively, with a mass density of 2.7g/cm^3. The discretization consisted of 24 elements within a cross section and 20 elements along the length of the beam. The first mode shape, seen in Figure 3-8, is first weak-axis bending.

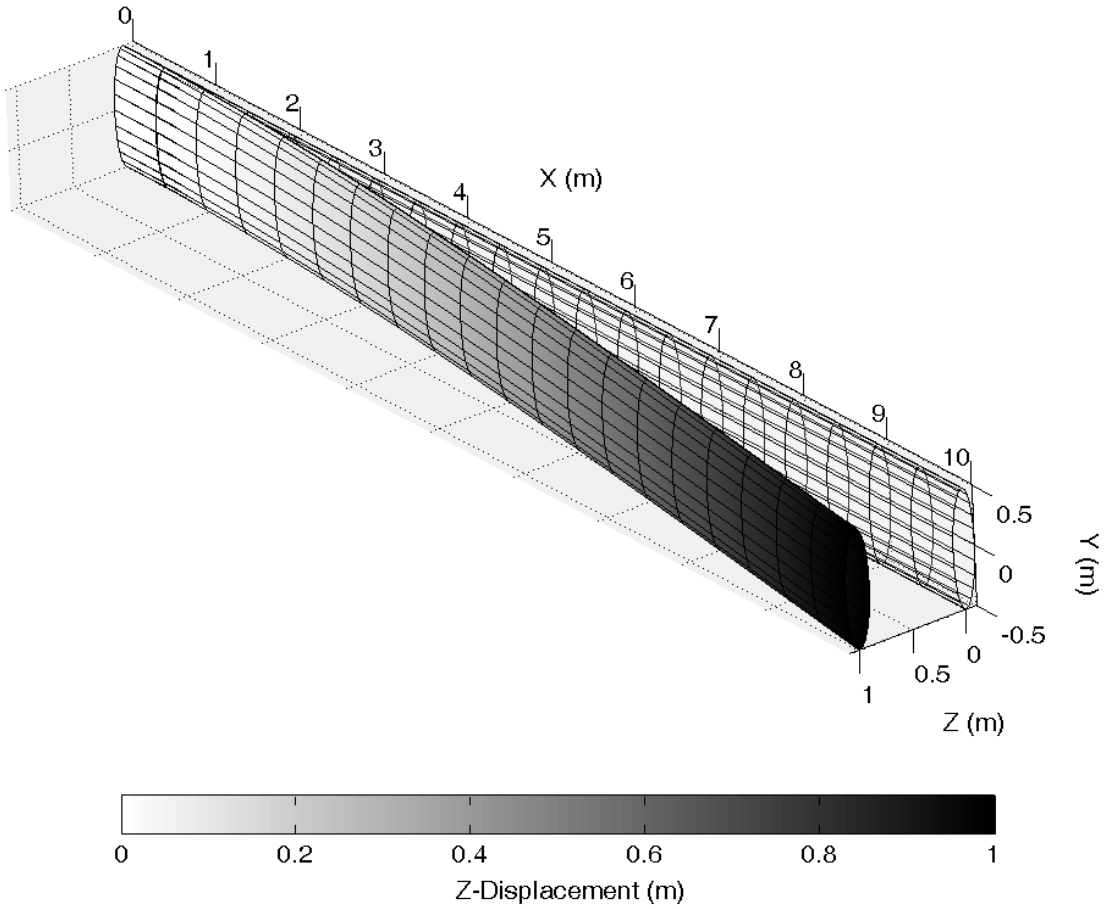

Figure 3-8: First Weak-Axis Bending

Numerical solutions exist for free transverse vibration of uniform Bernoulli-Euler beams with cantilever boundary conditions and were used for comparison with results obtained using the thin-walled beam model. The first two natural frequencies are given as **Error! Reference source not found.**:

$$\omega_1 = \frac{3.516}{L^2}\sqrt{\frac{EI}{\rho A}} \tag{3.6}$$

and

$$\omega_2 = \frac{22.03}{L^2}\sqrt{\frac{EI}{\rho A}} \tag{3.7}$$

where ω_1 is the first bending mode in either weak- or strong-axis depending on which area moment of inertia is chosen, and ω_2 is the second bending mode. The natural

frequencies ($f = \omega/2\pi$) in Hertz for the first three modes of vibration are presented in Table 3-3. They are compared there with those obtained using the thin-walled model of this thesis and the natural frequencies found for the test cylinder using a shell model with ABAQUS. The model used in ABAQUS was the 8-node quadratic shell elements with reduced integration and Lanczos method for calculating modes of vibration. For the cylinder, 28 elements around the perimeter of the cross section were used with 100 elements along the length of the beam which is a finer mesh than that used in this work, with significantly larger number of degrees of freedom. The mode shapes closely resembled those found using the thin-walled beam model, and are given in Figures B3-1 through B3-4 in Appendix B.

Table 3-3: Comparison of Natural Frequencies, *f* (Hz)

	Euler-Bernoulli Beam Theory	Shell Model	Thin-Walled Beam Model
Mode 1: First Weak-Axis Bending	2.332	2.277	2.249
Mode 2: First Strong-Axis Bending	8.228	8.476	8.434
Mode 3: Second Weak-Axis Bending	14.615	13.799	13.596
Mode 4: First Torsion	N/A	36.068	36.192

The natural frequencies for the first three modes obtained using the model presented in this work are in a closer agreement with those obtained with ABAQUS than those based on Euler-Bernoulli theory. The numerical results for the thin-walled beam model gave a first natural frequency of 2.249, which is less than a 2 percent error from the shell model. While there is more variation among higher modes with the thin-walled beam model, the third mode is still within 2 percent compared to the shell model. This is especially telling since the thin-walled beam model was able to obtain these results using 5 times fewer elements along the length of the beam and fewer nodes around the perimeter of the cross section. This is remarkable, given the difference in the number of

degrees of freedom is even bigger: 580 degrees of freedom in the thin-walled model (only 100 after elimination of δ's) versus 14,000 degrees of freedom in the shell model.

The first torsion mode is also well predicted by the thin-walled beam model, at 36.192 Hz, compared to the shell model results of 36.068 Hz. These results are especially telling, since the thin-walled beam model is able to obtain relatively accurate results for torsion, a mode that the Euler-Bernoulli beam theory cannot capture. Comparison of higher order modes is not very meaningful, because cross-sectional distortion present in the ABAQUS shell model is excluded in thin-walled models (and in real blades).

3.2.2 Forced Vibration

The second example for dynamic testing of the thin-walled beam model involved the same cylinder as studied in the previous example. This example, however, studies forced instead of free vibration. Specifically, an instantaneous load of 100 kN was applied to the free end of the beam in the *z*-direction (weak-axis direction) and sustained for the entire duration of the test. The Newmark-β Method, as described in Section 2.5.2, was used to find the system response, with the system starting at rest (zero initial displacements and velocities).

The application of the point load in the weak-axis direction induced a response shown in Figure 3-9. The amplitude of the response was approximately 1.785 meters compared to the beam theory maximum tip displacement of 1.885 meters given by $PL^3 / 3EI_y$. Additionally, about 4.5 cycles occurred over the 2 second interval, which is a frequency of 2.25Hz. Referring back to Table 3-3, a frequency of 2.25Hz is comparable to the natural frequency for the first mode of vibration (weak-axis bending). These are further indications that the thin-walled beam model is able to accurately predict a beam-like structure's behavior under dynamical loading.

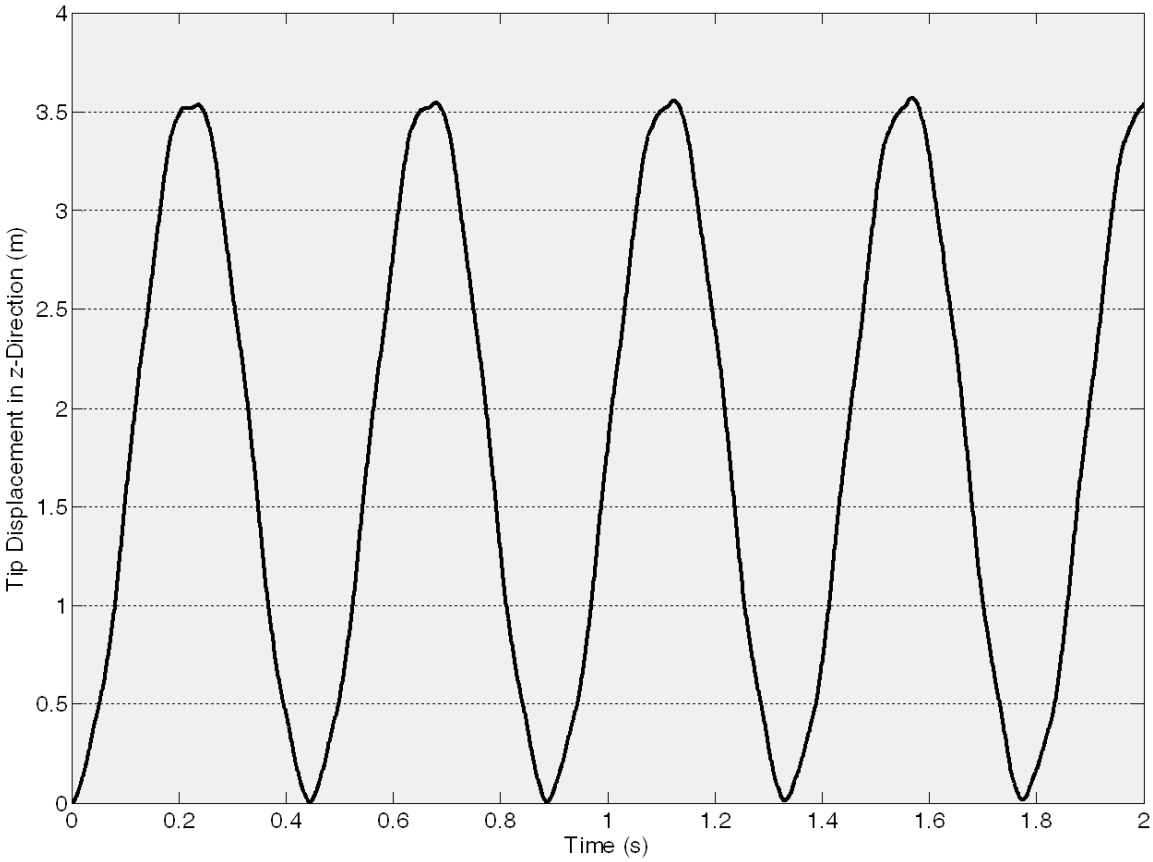

Figure 3-9: Tip Vibration

CHAPTER 4. CONCLUDING REMARKS AND FUTURE WORK

4.1 Summary

A computational model suitable for analysis of arbitrary thin-walled beams has been developed in this thesis. This includes beams whose cross section may have geometry as well as topology that vary along its length. An example of varying topology may include an internal wall that spans only a fragment of the beam's length, so the number of cells in the cross section may abruptly change.

The model also allows for beams containing different materials either along their length or within a cross section, or both. Each of the materials involved may be anisotropic. These features are particularly attractive in analysis of wind turbine blades.

The possibility of having anisotropic material properties is connected to the way warping is described in the presented model in that warping must be dependent on the particular distribution of the material in the cross section. In most existing models, warping functions are predetermined using either Saint Venant theory, if the cross sections are closed, or Vlasov theory, when the cross sections are open. This is typically done assuming that the beam is prismatic and composed of a single isotropic material. In addition, functions determined that way often exclude additional warping that is due to the presence of resultant transverse shear forces. While that process can theoretically be extended to problems of multiple materials, it would result in a significant amount of additional work to determine all of the associated cross-sectional properties. In this thesis, warping is described approximately by a discrete set of parameters associated with each cross section. The specific values of those parameters result from the system of governing equations, and it is those equations that implicitly define the form of the warping functions.

Finally, a key feature of the developed model is the fact that the deformation due to warping degrees of freedom (the δ's) is superimposed on the bending deformation, which dominates the overall response of the beam. It permits one to neglect the inertia

associated with those warping degrees of freedom without introducing any significant errors in the dynamic analysis. This, in turn, allows one to eliminate the warping degrees of freedom in dynamics and solve the fluid-structure interaction problem (where many solutions of the system are needed) with significantly reduced effort on the structural response side.

4.2 **Conclusions**

The research results presented here lead to the following main conclusions:

1. The approach adopted in this thesis leads to a model that indeed provides a good balance between simplicity and accuracy for beams with various topologies. The results obtained for a twisted beam with rectangular thin-walled cross sections (closed cross sections), I-beam (open cross sections), and beam with variable elliptical cross sections (closed cross sections) are comparing well with available results obtained independently.

2. The effects of various loading conditions are present in the model. For example, the results of the cantilevered twisted beam with tip loading, or the cantilevered I-beam under torsional moment are again in good agreement with available reference solutions.

3. Several conclusions can be drawn from comparison of the time-independent solutions for beams and shells.

a. It is clear that for the problems addressed in this thesis, the effects related to bending of the beam's walls are not significant. This conclusion is drawn from the comparison of the first four natural frequencies which are very close for the beam and shell solutions. Some of the higher order modes differ, but those, in shells, are related to the in-plane deformation of the cross section explicitly excluded in the beam model.

b. Significant reduction in the degrees of freedom provides results with good engineering accuracy. In the comparisons presented in this thesis, the number of degrees of freedom for the shell model was on the order of 14,000, while the model presented herein was of the order 500 (or 100 if the warping degrees of freedom are eliminated), and despite this difference, several lower order frequencies were still within one or two percent of each other.

4. The results provided in this thesis demonstrate that the two-dimensional stress analysis is perfectly adequate for analysis of thin-walled structures. Furthermore, representing the warping function by a set of discrete variables accurately describes the behavior of thin-walled beams with

a. Non-prismatic geometry

b. Multicellular cross sections

c. Multiple anisotropic material properties

4.3 **Towards Fluid-Structure Interaction**

In the previous chapter, the accuracy of the thin-walled beam model was established through various loading examples including static bending and torsion, as well as free and forced vibration. While this model provides the structural framework for the modeling of structures such as wind turbine blades, a fluid mechanics model is also necessary to accurately predict loading conditions. To date, both models exist independently, but further work remains in coupling the two codes for full fluid-structure interaction.

Ultimately, the two models will be fully integrated so that the fluid mechanics model provides the input (pressures on the structure) to the thin-walled beam model which subsequently measures the response (deformations). In each timestep thereafter, this response is fed back into the fluids model where new pressures are calculated and inputted into the structural model for the new response, and so on. Ultimate validation of this model, as explained in the Introduction, will be in the comparison of data obtained from the 2.5 MW wind turbine "Liberty" that is being constructed at the University of Minnesota's UMore Park.

BIBLIOGRAPHY

[1] B.Z. Vlasov, "Thin-Walled Elastic Bars." *Fizmatgiz*. Moscow (1959).

[2] V.Z. Vlasov, "Thin-Walled Elastic Beams." *Israel Program for Scientific Translations.* Jerusalem (1961).

[3] A. Saleeb, A. Gendy, "Shear-flexible models for spatial buckling of thin-walled curved beams." *International Journal for Numerical Methods in Engineering*, **31** (1991) 729-757.

[4] G. Romano, L. Rosati, G. Ferro, "Shear deformability of thin-walled beams with arbitrary cross sections." *International Journal for Numerical Methods in Engineering,* **35** (1992) 283-306.

[5] R.D. Ambrosini, J.D. Riera, R.F. Danesi. "Dynamic Analysis of Thin-walled and Variable Open Section Beams with Shear Flexibility." *International Journal for Numerical Methods in Engineering,* **38** (1995) 2867-2885.

[6] J.W. Wekezer, "Elastic torsion of thin walled bars of variable cross sections." *Computers & Structures,* **19** (1984) 401-407.

[7] H.R. Ronagh, M.A. Bradford, M.M. Attard, "Nonlinear analysis of thin-walled members of variable cross section. Part I: Theory." *Computers & Structures,* **77** (2000) 285-299.

[8] H.R. Ronagh, M.A. Bradford, M.M. Attard, "Nonlinear analysis of thin-walled members of variable cross section. Part II: Application." *Computers & Structures,* **77** (2000) 301-313.

[9] Z. Yao, K.J.R. Rasmussen, "Material and geometric nonlinear isoparametric spline finite strip analysis of perforated thin-walled steel structures – Analytical developments." *Thin-Walled Structures,* **49** (2011) 1359-1373.

[10] L. Librescu, O. Song, *Thin-Walled Composite Beams*. Springer, 1st ed., (2006).

[11] M.T. Piovan, V.H. Cortínez, "Mechanics of thin-walled curved beams made of composite materials, allowing for shear deformability." *Thin-Walled Structures*, **45** (2007) 759-789.

[12] Z. Zamani, H. Haddadpour, M.R. Ghazavi, "Curvilinear fiber optimization tools for design thin walled beams." *Thin-Walled Structures,* **49** (2011) 448-454.

[13] "About." *EOLOS Wind Energy Research Consortium*. Regents of the University of Minnesota, (2010). <www.eolos.umn.edu/about>.

[14] J. Locke, U. Valencia, "Design Studies for Twist-Coupled Wind Turbine Blades." Sandia National Laboratories, Report SAND2004-0522, (2004).

[15] Y. Bazilevs, M.-C. Hsu, I. Akkerman, S. Wright, K. Takizawa, B. Henicke, T. Spielman, T.E. Tezduyar, "3D simulation of wind turbine rotors at full scale. Part I: Geometry modeling and aerodynamics." *International Journal for Numerical Methods in Fluids,* **65** (2011) 207-235.

[16] Y. Bazilevs, M.-C. Hsu, J. Kiendl, R. Wüchner, K.-U. Bletzinger, "3D simulation of wind turbine rotors at full scale. Part II: Fluid-structure interaction modeling with composite blades." *International Journal for Numerical Methods in Fluids,* **65** (2011) 236-253.

[17] A.C. Ugural, S.K. Fenster, *Advanced Strength and Applied Elasticity*. Prentice Hall PTR, 4th ed., (2003).

[18] T.J.R. Hughes, T.E. Tezduyar, "Finite elements based upon Mindlin plate theory with particular reference to the four-node bilinear isoparametric element." *Journal of Applied Mechanics,* **48** (1981) 587-596.

[19] E.N. Dvorkin, K.J. Bathe, "A continuum mechanics based four-node shell element for general nonlinear analysis." *Engineering Computations,* **1** (1984) 77-88.

[20] B.D. Agarwal, L.J. Broutman, K. Chandrashekhara. *Analysis and Performance of Fiber Composites*. John Wiley & Sons, 3rd ed., (2006).

[21] R.R. Craig, A.J. Kurdila, *Fundamentals of Structural Dynamics*. John Wiley & Sons, 2nd ed., (2006).

DETAILS OF STRAIN EVALUATION

A1. Displacement Fields Due to Torsion and Warping

Evaluating the strains due to warping and torsion, each element of the discretized beam surface is treated as a membrane. In this thesis the displacement field within those elements is approximated using bilinear functions

$$\mathbf{u}(\xi,\eta)=\begin{Bmatrix} u_x(\xi,\eta) \\ u_y(\xi,\eta) \\ u_z(\xi,\eta) \end{Bmatrix}=\begin{Bmatrix} \sum_{I=1}^{4} u_{Ix} N_I(\xi,\eta) \\ \sum_{I=1}^{4} u_{Iy} N_I(\xi,\eta) \\ \sum_{I=1}^{4} u_{Iz} N_I(\xi,\eta) \end{Bmatrix} \tag{A.1}$$

where u_{Ix} u_{Iy} and u_{Iz} are the displacement components at node I and functions $N_I(\xi,\eta)$ are specified in Eq. (2.2). The nodal values of displacements are related to torsional rotation and warping as follows

$$\begin{Bmatrix} u_{Ix} \\ u_{Iy} \\ u_{Iz} \end{Bmatrix}=\begin{Bmatrix} \delta_I \\ -z_I\,\theta_x \\ y_I\theta_x \end{Bmatrix} \tag{A.2}$$

A2. Strains Due to Torsion and Warping

The shape of the membrane element described in Eq. (2.1) can also be presented in the following form

$$\mathbf{R}(\xi,\eta) = \sum_{\mathrm{I}=1}^{4} \mathbf{R_I}\, \mathrm{N_I}(\xi,\eta) \tag{A.3}$$

where $\mathbf{R}(\xi,\eta)$ is the position vector of any point within the element, $\mathbf{R}_\mathrm{I}$ are position vectors of the element nodes, and $\mathrm{N_I}(\xi,\eta)$ are bilinear approximating functions (of Eq. (2.2)).

In the curvilinear (ξ,η) coordinate system, the (covariant) components of the membrane strain tensors are defined as

$$\boldsymbol{\varepsilon}_{\alpha\beta} = \frac{1}{2}\left(\mathbf{u}_{,\alpha} \bullet \mathbf{G}_{\beta} + \mathbf{u}_{,\beta} \bullet \mathbf{G}_{\alpha}\right) \tag{A.4}$$

with $\alpha,\beta \in \{1,2\} = \{\xi,\eta\}$. Locally, those strain components are related to the vectors $\mathbf{G}^{\alpha}$, α = 1,2, tangent to the surface of the element and coupled to the vectors $\mathbf{G}_{\alpha}$, α = 1,2, (also tangent to the surface of the element) readily computable given the position vector $\mathbf{R}(\xi,\eta)$ specified in Eq. (2.1).

$$\mathbf{G_1} = \mathbf{R}_{,\xi} = \begin{Bmatrix} \sum_{\mathrm{I}=1}^{4} x_\mathrm{I}\, \mathrm{N}_{\mathrm{I},\xi} \\ \sum_{\mathrm{I}=1}^{4} y_\mathrm{I}\, \mathrm{N}_{\mathrm{I},\xi} \\ \sum_{\mathrm{I}=1}^{4} z_\mathrm{I}\, \mathrm{N}_{\mathrm{I},\xi} \end{Bmatrix} = \begin{Bmatrix} \mathrm{G}_{1x} \\ \mathrm{G}_{1y} \\ \mathrm{G}_{1z} \end{Bmatrix}$$

$$\mathbf{G_2} = \mathbf{R}_{,\eta} = \begin{Bmatrix} \sum_{\mathrm{I}=1}^{4} x_\mathrm{I}\, \mathrm{N}_{\mathrm{I},\xi} \\ \sum_{\mathrm{I}=1}^{4} y_\mathrm{I}\, \mathrm{N}_{\mathrm{I},\xi} \\ \sum_{\mathrm{I}=1}^{4} z_\mathrm{I}\, \mathrm{N}_{\mathrm{I},\xi} \end{Bmatrix} = \begin{Bmatrix} \mathrm{G}_{2x} \\ \mathrm{G}_{2y} \\ \mathrm{G}_{2z} \end{Bmatrix} \tag{A.5}$$

by the following orthogonality conditions

$$\mathbf{G}_{\alpha} \bullet \mathbf{G}^{\beta} = \delta_{\alpha}^{\beta} \quad , \quad \delta_{\alpha}^{\beta} = \begin{cases} 0, \alpha \neq \beta \\ 1, \alpha = \beta \end{cases} \tag{A.6}$$

Due to the assumptions made in this model, the bending-related strain, introduced in Eq. (2.15) has only one non-vanishing component, ε_{xx}. For a general geometry of the beam, axis *x* is not parallel to any vector tangent to the surface of a typical element. Thus, the two-dimensional strain components of Eq. (A.4), which are tangent to that surface, are evaluated in a different coordinate system than those due to bending. To be able to combine them, the components of Eq. (A.4) are transformed to an orthogonal system including axis *x*, and two other axes orthogonal to *x*, one of which is tangent to the surface of the element. The nature of this transformation is three-dimensional thus, first, the strains state due to warping and torsion need to be represented by an *equivalent* three-dimensional state.

The two-dimensional stress state of Eq. (A.4) can be viewed as a three-dimensional state if the unit vector $\boldsymbol{n}$ (=$\mathbf{G^3}$), normal to the surface of the element is added to the two tangent vectors $\mathbf{G^{\alpha}}$ defined by Eqs. (A.5) and (A.6). To achieve that, one needs to assume $\varepsilon_{\alpha 3}$= ε_{33}=0. Thus, the components of a three-dimensional strain state equivalent to that of Eq. (A.4) can be written as

$$\boldsymbol{\varepsilon}_{\Gamma\Delta} = \delta^{\alpha}_{\Gamma}\delta^{\beta}_{\Delta}\boldsymbol{\varepsilon}_{\alpha\beta} = \frac{1}{2}\delta^{\alpha}_{\Gamma}\delta^{\beta}_{\Delta}\left(\mathbf{u}_{,\boldsymbol{\alpha}} \bullet \boldsymbol{G}_{\boldsymbol{\beta}} + \mathbf{u}_{,\boldsymbol{\beta}} \bullet \boldsymbol{G}_{\boldsymbol{\alpha}}\right) \tag{A.7}$$

where $\Gamma,\Delta \in \{1,2,3\}$, $\alpha,\beta \in \{1,2\}$ and, as in Eq. (A.6), δ^{α}_{Γ} is the Kronecker "delta" symbol.

Considering the way the beams are discretized in this work, the nodes 1 and 4 as well as 2 and 3 of a typical element are always located in two planes perpendicular to the *x*-axis. For the bilinear approximation (used here) this implies that, at every point of the element, the vector $\mathbf{G_2} = \mathbf{R}_{,\eta}$ is perpendicular to the *x*-axis (and tangent to the element surface). Thus, if the three-dimensioned strain state of Eq. (A.7) is transformed to the coordinate system specified by vectors $\left\{\mathbf{i}, \frac{\mathbf{G_2}}{|\mathbf{G_2}|}, \mathbf{N}\right\} = \{\mathbf{e_1}, \mathbf{e_2}, \mathbf{e_3}\}$ where **i** is a (unit) vector parallel to the *x*-axis and $\mathbf{e_2}$, $\mathbf{e_3}$ are unit vectors such that

$$\mathbf{e_3} = \mathbf{N} = \mathbf{e_1} \times \mathbf{e_2} \tag{A.8}$$

the *x*-components of the bending related strain and torsion/warping-related strains can be combined.

The transformation of the strain components of Eq. (A.7) relating the vector basis $\mathbf{G^1},\mathbf{G^2},\mathbf{G^3}=\boldsymbol{n}$ to the components related to the vector basis $\mathbf{i},\mathbf{G_2},\mathbf{N}$ will be achieved in the following two steps.

i. Transformation of the components $\varepsilon_{\Gamma\Delta}$ of Eq. (A.7) related to $\mathbf{G^1},\mathbf{G^2},\mathbf{G^3}=\boldsymbol{n}$ to $\varepsilon^{\Gamma\Delta}$ related to the vectors $\mathbf{G_1},\mathbf{G_2},\mathbf{G^3}=\boldsymbol{n}=\mathbf{G_3}$. Note that one of these new set of vectors is $\mathbf{G_2}$ that is needed in the final set $\mathbf{i},\mathbf{G_2},\mathbf{N}$.

ii. Transformation of the components obtained in step i) to the components, $\hat{\varepsilon}^{\Gamma\Delta}$, related to $\mathbf{e_1},\mathbf{e_2},\mathbf{e_3}$.

Denoting the strain components related to the vector set $\mathbf{G_1},\mathbf{G_2},\mathbf{G^3}=\boldsymbol{n}=\mathbf{G_3}$ by $\varepsilon^{\Gamma\Delta}$, $\Gamma,\Delta\in\{1,2,3\}$, the $\varepsilon^{\alpha\beta}$, $\alpha,\beta\in\{1,2\}$ part of it can be computed by the formula

$$\begin{bmatrix}\varepsilon^{11} & \varepsilon^{12}\\ \varepsilon^{12} & \varepsilon^{22}\end{bmatrix}=\begin{bmatrix}\mathrm{G}^{11} & \mathrm{G}^{12}\\ \mathrm{G}^{12} & \mathrm{G}^{22}\end{bmatrix}\begin{bmatrix}\varepsilon_{11} & \varepsilon_{12}\\ \varepsilon_{12} & \varepsilon_{22}\end{bmatrix}\begin{bmatrix}\mathrm{G}^{11} & \mathrm{G}^{12}\\ \mathrm{G}^{12} & \mathrm{G}^{22}\end{bmatrix} \tag{A.9}$$

where

$$\begin{bmatrix}\mathrm{G}^{11} & \mathrm{G}^{12}\\ \mathrm{G}^{12} & \mathrm{G}^{22}\end{bmatrix}=\begin{bmatrix}\mathrm{G}_{11} & \mathrm{G}_{12}\\ \mathrm{G}_{12} & \mathrm{G}_{22}\end{bmatrix}^{-1}=\frac{1}{J^2}\begin{bmatrix}\mathrm{G}_{22} & -\mathrm{G}_{12}\\ -\mathrm{G}_{12} & \mathrm{G}_{11}\end{bmatrix} \tag{A.10}$$

with

$$\begin{aligned}\mathrm{G}_{11}&=\mathbf{R}_{,\xi}\bullet\mathbf{R}_{,\xi}=\mathbf{G_1}\bullet\mathbf{G_1}\\ \mathrm{G}_{12}&=\mathbf{R}_{,\xi}\bullet\mathbf{R}_{,\eta}=\mathbf{G_1}\bullet\mathbf{G_2}\\ \mathrm{G}_{22}&=\mathbf{R}_{,\eta}\bullet\mathbf{R}_{,\eta}=\mathbf{G_2}\bullet\mathbf{G_2}\\ J^2&=\mathrm{G}_{11}\mathrm{G}_{22}-\left(\mathrm{G}_{12}\right)^2\end{aligned} \tag{A.11}$$

Further evaluation of Eq. (A.9) yields

$$\begin{aligned}\varepsilon^{11}&=\varepsilon_{11}\left(\mathrm{G}^{11}\right)^2+2\varepsilon_{12}\left(\mathrm{G}^{11}\mathrm{G}^{21}\right)+\varepsilon_{22}\left(\mathrm{G}^{21}\right)^2\\ \varepsilon^{12}&=\varepsilon_{11}\left(\mathrm{G}^{11}\mathrm{G}^{12}\right)+\varepsilon_{12}\left(\mathrm{G}^{11}\mathrm{G}^{22}+\mathrm{G}^{12}\mathrm{G}^{12}\right)+\varepsilon_{22}\left(\mathrm{G}^{12}\mathrm{G}^{22}\right)\\ \varepsilon^{11}&=\varepsilon_{11}\left(\mathrm{G}^{12}\right)^2+2\varepsilon_{12}\left(\mathrm{G}^{12}\mathrm{G}^{22}\right)+\varepsilon_{22}\left(\mathrm{G}^{22}\right)^2\end{aligned} \tag{A.12}$$

Additionally, $\varepsilon^{13}=\varepsilon^{23}=\varepsilon^{33}=0$.

The second step (step ii) is similar and involves the following transformation

$$\begin{bmatrix} \hat{\varepsilon}^{11} & \hat{\varepsilon}^{12} & \hat{\varepsilon}^{13} \\ \hat{\varepsilon}^{12} & \hat{\varepsilon}^{22} & \hat{\varepsilon}^{23} \\ \hat{\varepsilon}^{13} & \hat{\varepsilon}^{23} & \hat{\varepsilon}^{33} \end{bmatrix} = \mathbf{A}^{\mathrm{T}} \begin{bmatrix} \varepsilon^{11} & \varepsilon^{12} & \varepsilon^{13} \\ \varepsilon^{12} & \varepsilon^{22} & \varepsilon^{23} \\ \varepsilon^{13} & \varepsilon^{23} & \varepsilon^{33} \end{bmatrix} \mathbf{A} \tag{A.13}$$

where

$$\mathbf{A} = \begin{bmatrix} \mathbf{G_1} \bullet \boldsymbol{e_1} & \mathbf{G_1} \bullet \boldsymbol{e_2} & \mathbf{G_1} \bullet \boldsymbol{e_3} \\ \mathbf{G_2} \bullet \boldsymbol{e_1} & \mathbf{G_2} \bullet \boldsymbol{e_2} & \mathbf{G_2} \bullet \boldsymbol{e_3} \\ \mathbf{G_3} \bullet \boldsymbol{e_1} & \mathbf{G_3} \bullet \boldsymbol{e_2} & \mathbf{G_3} \bullet \boldsymbol{e_3} \end{bmatrix} \tag{A.14}$$

Evaluation of the vectors in the above expressions and performing the operations involved there leads to the following result

$$\begin{aligned} \hat{\varepsilon}_{xx} &= \hat{\varepsilon}_{11} = \left(\mathrm{G}_{1x}\right)^2 \varepsilon^{11} \\ \hat{\varepsilon}_{xy} &= \hat{\varepsilon}_{12} = \left(\beta_{12}\varepsilon^{11} + \varepsilon^{12}\right)\mathrm{G}_{1x}\sqrt{\mathrm{G}_{22}} \end{aligned} \tag{A.15}$$

which are the only components relevant in the theory developed herein. Variables in Eq. (A.15) involve components of vectors $\mathbf{G_1}$ and $\mathbf{G_2}$ which are computed as in Eq. (A.5) and with

$$\beta_{12} = \frac{\mathrm{G}_{1y}\mathrm{G}_{2y} + \mathrm{G}_{1z}\mathrm{G}_{2z}}{\mathrm{G}_{22}} \tag{A.16}$$

A3. Finite Element Approximation of Warping/Torsion-Related Strains

If the vector of nodal displacements is grouped in the following fashion

$$\mathbf{d_u}^{\mathrm{T}} = \left\{\mathbf{u_1}^{\mathrm{T}}, \mathbf{u}_2^{\mathrm{T}}, \mathbf{u}_3^{\mathrm{T}}, \mathbf{u}_4^{\mathrm{T}}\right\} \quad , \quad \mathbf{u_I}^{\mathrm{T}} = \left\{u_{Ix}, u_{Iy}, u_{Iz}\right\} \tag{A.17}$$

the finite element approximation of components $\varepsilon_{\alpha\beta}$ defined in Eq. (A.4) is

$$\begin{aligned} \varepsilon_{11} &= \left\{\mathbf{B}_{\mathbf{11}}^1, \mathbf{B}_{\mathbf{11}}^2, \mathbf{B}_{\mathbf{11}}^3, \mathbf{B}_{\mathbf{11}}^4\right\}\mathbf{d_u} = \mathbf{B_{11}}\mathbf{d_u} \\ \varepsilon_{12} &= \left\{\mathbf{B}_{\mathbf{12}}^1, \mathbf{B}_{\mathbf{12}}^2, \mathbf{B}_{\mathbf{12}}^3, \mathbf{B}_{\mathbf{12}}^4\right\}\mathbf{d_u} = \mathbf{B_{12}}\mathbf{d_u} \\ \varepsilon_{22} &= \left\{\mathbf{B}_{\mathbf{22}}^1, \mathbf{B}_{\mathbf{22}}^2, \mathbf{B}_{\mathbf{22}}^3, \mathbf{B}_{\mathbf{22}}^4\right\}\mathbf{d_u} = \mathbf{B_{22}}\mathbf{d_u} \end{aligned} \tag{A.18}$$

where

$$\begin{aligned} \mathbf{B}_{\mathbf{11}}^{\mathrm{I}} &= \left\{G_{1x}N_{\mathrm{I},\xi}, G_{1y}N_{\mathrm{I},\xi}, G_{1z}N_{\mathrm{I},\xi}\right\} \\ \mathbf{B}_{\mathbf{12}}^{\mathrm{I}} &= \left\{G_{1x}N_{\mathrm{I},\eta} + G_{2x}N_{\mathrm{I},\xi}, G_{1y}N_{\mathrm{I},\eta} + G_{2y}N_{\mathrm{I},\xi}, G_{1z}N_{\mathrm{I},\eta} + G_{22}N_{\mathrm{I},\xi}\right\} \\ \mathbf{B}_{\mathbf{22}}^{\mathrm{I}} &= \left\{G_{2x}N_{\mathrm{I},\eta}, G_{2y}N_{\mathrm{I},\eta}, G_{2z}N_{\mathrm{I},\eta}\right\} \end{aligned} \tag{A.19}$$

Consequently, in view of Eqs. (A.12) and (A.15), the following matrix formulas can be deduced

$$\begin{aligned} \hat{\varepsilon}_{11} &= \hat{\mathbf{B}}_{\mathbf{11}}\mathbf{d_u} \\ \hat{\varepsilon}_{12} &= \hat{\mathbf{B}}_{\mathbf{12}}\mathbf{d_u} \end{aligned} \tag{A.20}$$

where

$$\begin{aligned} \hat{\mathbf{B}}_{\mathbf{11}} &= A_1\mathbf{B_{11}} + A_2\mathbf{B_{12}} + A_3\mathbf{B_{22}} \\ \hat{\mathbf{B}}_{\mathbf{12}} &= C_1\mathbf{B_{11}} + C_2\mathbf{B_{12}} + C_3\mathbf{B_{22}} \end{aligned} \tag{A.21}$$

with

$$\begin{aligned} A_1 &= \left(G_{1x}\right)^2\left(G_{11}\right)^2 \\ A_2 &= 2\left(G_{1x}\right)^2 G^{11}G^{21} \\ A_3 &= \left(G_{1x}\right)^2\left(G_{21}\right)^2 \\ C_1 &= G_{1x}\sqrt{G_{22}}\left[\beta_{12}\left(G^{11}\right)^2 + G^{11}G^{12}\right] \\ C_2 &= G_{1x}\sqrt{G_{22}}\left[2\beta_{12}G^{11}G^{21} + G^{11}G^{21} + \left(G^{12}\right)^2\right] \\ C_3 &= G_{1x}\sqrt{G_{22}}\left[\beta_{12}\left(G^{12}\right)^2 + G^{12}G^{22}\right] \end{aligned} \tag{A.22}$$

Finally, Eq. (A.2) – used in an elementary way for all 4 nodes of the element – renders the following relation

$$\mathbf{d_u} = \mathbf{T}\mathbf{d}_e \tag{A.23}$$

where $\mathbf{T}$ is the transformation matrix of size 12 by 14, $\mathbf{d_u}$ is specified in Eq. (A.17) and $\mathbf{d}_e$ in Eq. (2.1). Using this relation in Eq. (A.20) transforms it to the following form

$$\begin{aligned} \hat{\varepsilon}_{11} &= \hat{\mathbf{B}}_{11}\mathbf{d_u} = \hat{\mathbf{B}}_{11}\mathbf{T}\mathbf{d}_e = \tilde{\mathbf{B}}_{11}\mathbf{d}_e \\ \hat{\varepsilon}_{12} &= \hat{\mathbf{B}}_{12}\mathbf{d_u} = \hat{\mathbf{B}}_{12}\mathbf{T}\mathbf{d}_e = \tilde{\mathbf{B}}_{12}\mathbf{d}_e \end{aligned} \tag{A.24}$$

which are combined with the bending-related part in Eq. (2.22) of the main body of the thesis.

ADDITIONAL TESTING CALCULATIONS

B1. Parameters used in Static Test Calculations

The analytical solutions for the tip displacements of the twisted beam given previously are solved as follows. First, since the moment of inertia of a rectangle about the centroid is given as

$$I = \frac{bh^3}{12} \tag{B.1}$$

the moment of inertia of our thin-walled rectangle about the z-axis is calculated as

$$\begin{aligned} I_z &= \frac{1}{12}\left[(b+t)(h+t)^3 - (b-t)(h-t)^3\right] \\ &= \frac{1}{12}\left[(4+0.2)(12+0.2)^3 - (4-0.2)(12-0.2)^3\right] m^4 \\ &= 115.25 m^4 \end{aligned} \tag{B.2}$$

similarly, the moment of inertia about the y-axis is

$$\begin{aligned} I_y &= \frac{1}{12}\left[(h+t)(b+t)^3 - (h-t)(b-t)^3\right] \\ &= 21.36 m^4 \end{aligned} \tag{B.3}$$

B2. Parameters used in Dynamic Test Calculations

For the computation of the theoretical natural frequencies of the elliptical cylinder, several quantities need to be calculated based on the geometries and material properties chosen. First, the second (mass) moment of inertia about the y-axis for an ellipse is given as

$$I_y = \frac{\pi b a^3}{4} \tag{B.4}$$

so, for our thin-walled ellipse the moment of inertia is calculated as

$$\begin{aligned} I_y &= \frac{\pi}{4}\left[\left(b+\frac{t}{2}\right)\left(a+\frac{t}{2}\right)^3 - \left(b-\frac{t}{2}\right)\left(a-\frac{t}{2}\right)^3\right] \\ &= \frac{\pi}{4}\left[(0.5+0.01)(0.1+0.01)^3 - (0.5-0.01)(0.1-0.01)^3\right] m^4 \\ &= 2.5258 \text{x} 10^{-4}\, m^4 \end{aligned} \tag{B.5}$$

similarly, the moment of inertia about the z-axis is

$$I_z = \frac{\pi}{4}\left[\left(a+\frac{t}{2}\right)\left(b+\frac{t}{2}\right)^3 - \left(a-\frac{t}{2}\right)\left(b-\frac{t}{2}\right)^3\right] \quad \text{(B.6)}$$
$$= 3.1441\text{x}10^{-3}\,m^4$$

Next, the mass per unit length is calculated as

$$m = \pi\left[\left(a+\frac{t}{2}\right)\left(b+\frac{t}{2}\right) - \left(a-\frac{t}{2}\right)\left(b-\frac{t}{2}\right)\right]\rho$$
$$= \pi\left[(0.1+0.01)(0.5+0.01) - (0.1-0.01)(0.5-0.01)\right]m^2\left(2700\frac{kg}{m^3}\right) \quad \text{(B.7)}$$
$$= 101.7876\frac{kg}{m}$$

Substituting these variables into Eq. ((3.6) for the first weak-axis bending natural frequency, we obtain

$$\omega_{1y} = (1.875)^2\sqrt{\frac{EI_y}{mL^4}}$$
$$= (1.875)^2\sqrt{\frac{70\text{x}10^9\,Pa\left(2.5258\text{x}10^{-4}\,m^4\right)}{101.7876\frac{kg}{m}(10m)^4}} \quad \text{(B.8)}$$
$$= 14.65\frac{rad}{s}\left(\frac{cycle}{2\pi rad}\right)$$
$$= 2.332Hz$$

Similarly, the first strong-axis bending natural frequency is

$$\omega_{1z} = (1.875)^2\sqrt{\frac{EI_z}{mL^4}} = 8.228\text{Hz} \quad \text{(B.9)}$$

and lastly, the second weak-axis bending natural frequency (from Eq.((3.7)) is

$$\omega_{2y} = (4.694)^2\sqrt{\frac{EI_y}{mL^4}} = 14.615\text{Hz} \quad \text{(B.10)}$$

B3. Additional Dynamic Tests Results from Shell Model using ABAQUS

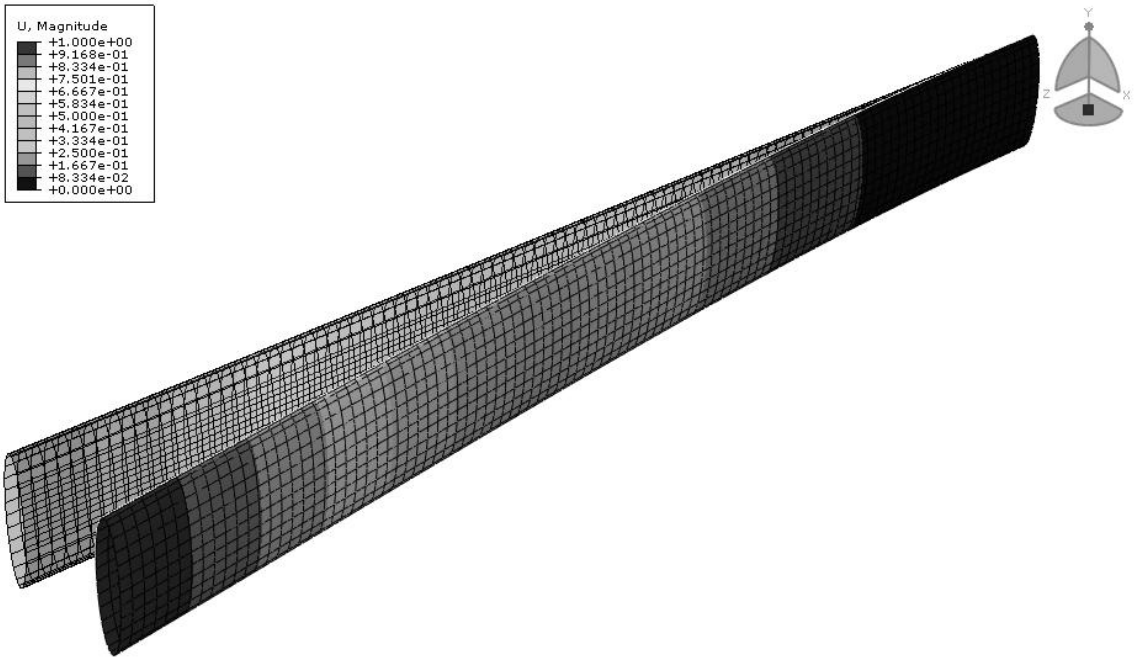

Figure B3-1: Mode 1, First Weak-Axis Bending

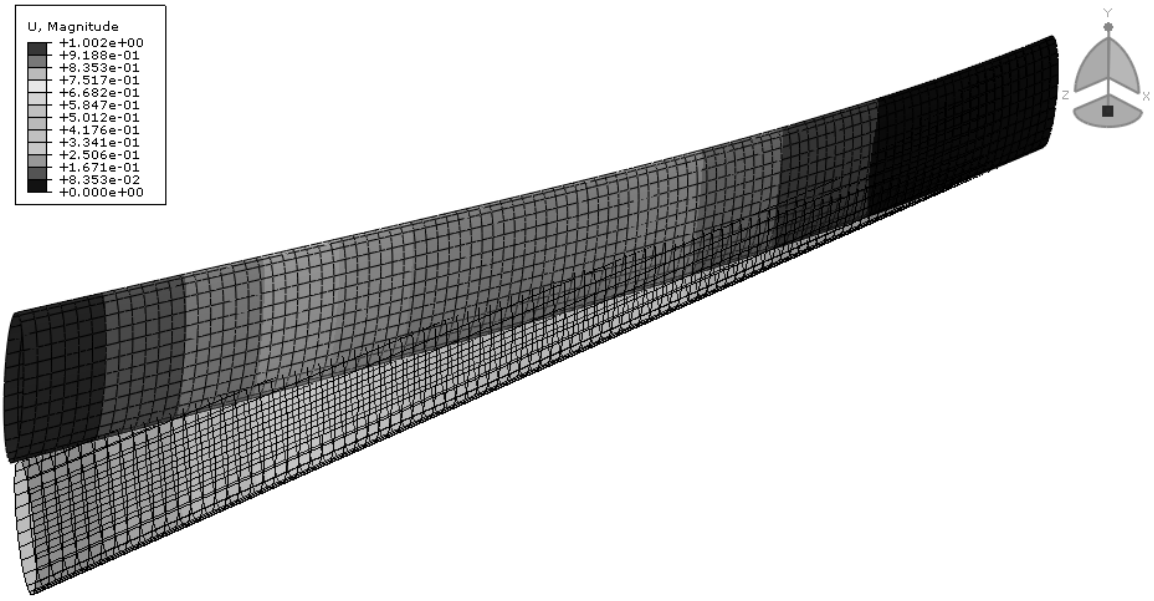

Figure B3-2: Mode 2, First Strong-Axis Bending

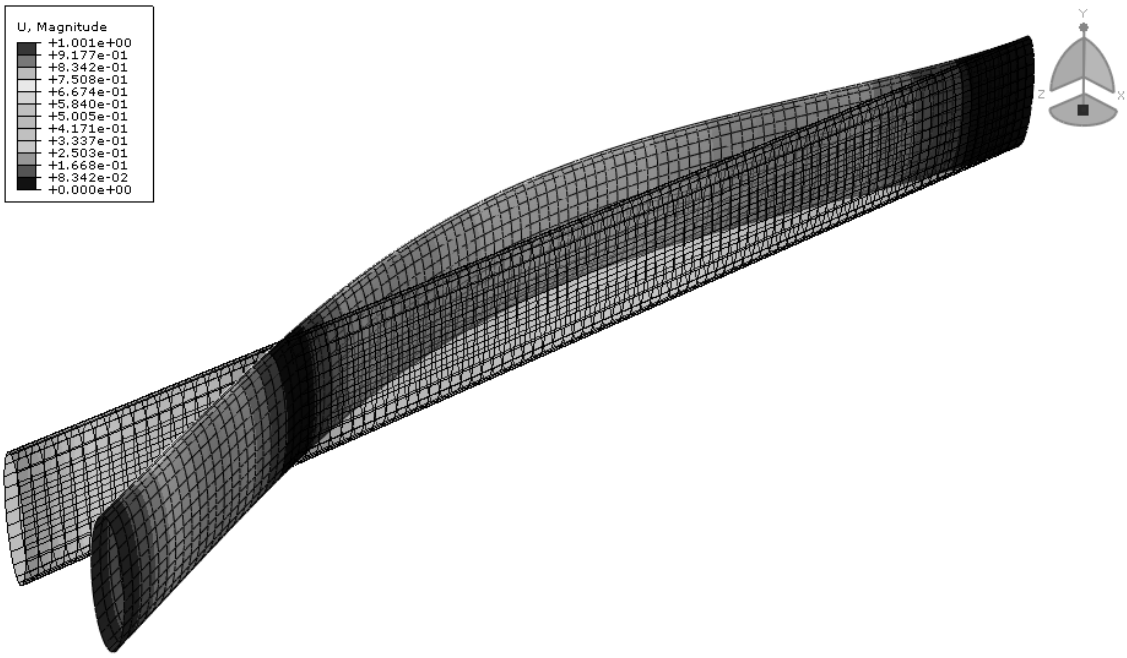

Figure B3-3: Mode 3, Second Weak-Axis Bending

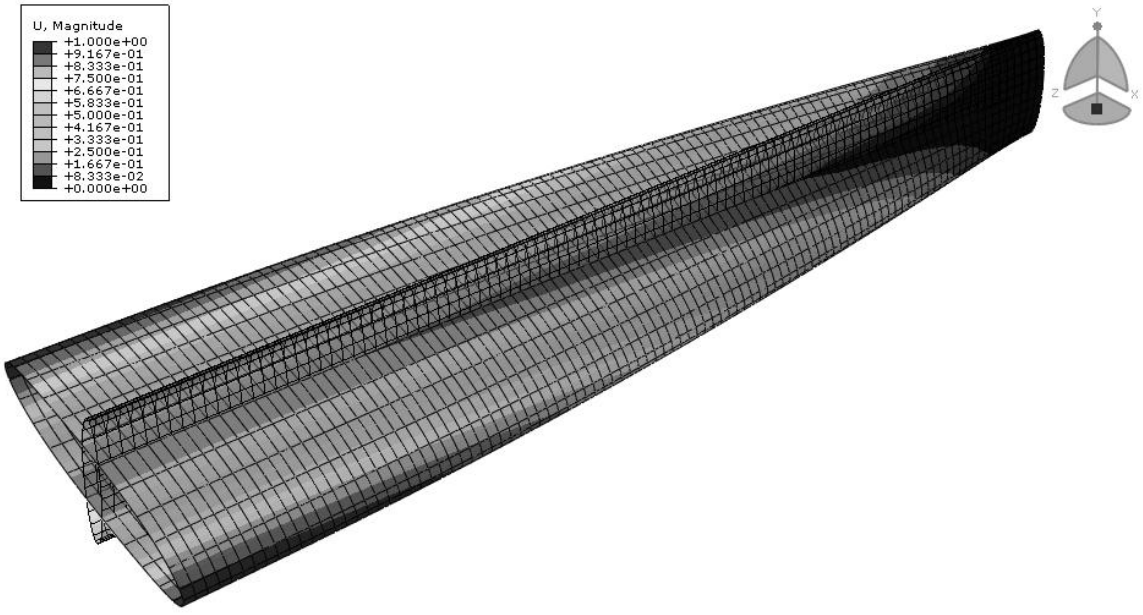

Figure B3-4: Mode 4, First Torsion